POLITECNICO DI TORINO

Tesi di Laurea Magistrale in Ingegneria Meccanica

Fracture Toughness Assessment using Digital Image Correlation in Additive Manufacturing

Relatori
Prof. E. Brusa
Prof. J. Gardan
Prof. A. Makke
Prof. N. Recho

Studente
A. Lenti

Luglio 2019

Abstract

The core topic of this work is the implementation of a numerical algorithm to measure the fracture toughness of a bending sample using Digital Image Correlation (DIC) and its application to the products of an optimized printing technique for Fused Deposition Modeling (FDM). In order to enhance the mechanical resistance of specimens of acrilonitrile butadiene stirene (ABS) printed with a conventional thread deposition of FDM, this innovative printing method suggests a new layer's configuration where the polymeric filament is placed following the principal stress directions within the layered structure [1], previously computed through a finite element (FE) simulation. The overall objectives are both to present an alternative method to calculate the Stress Intensity Factor (SIF), using a Monte Carlo (MC) computational approach, and to characterize the mechanical enhancements ensured by the optimized filament deposition. The study has been carried out through the analysis of the outcomes of previous three points bending tests [2] and through the comparison of the numerical results of the two specimen's types. The bending specimens used, dimensioned according to Thogo and Ishii's work [3], are of the type Single Edge Notched Beam (SENB) and were printed and tested in order to investigate the influence of the thread deposition on the fracture toughness in a mode I loading case. The DIC analysis has been extensively used to investigate the superficial displacement and strain fields around the notch tip to study the crack growth's features and to detect the crack onset. The gathered data were necessary to the implementation of a Monte Carlo computational algorithm that has been employed to calculate the critical SIF by fitting the displacement field measured by DIC, with Williams-Westergaard's analytical model. Therefore an assessment of the fracture toughness enhancement was possible: the comparison between optimized and conventional specimens shows a clear resistance improvement obtained with the new configuration, which leads to a gain in terms of K_{Ic} of up to almost 15% on average. Additive Manufacturing (AM) is increasingly gaining importance not only in prototyping but also in industrial production [4], hence the optimization of the technologies involved and the enhancement of some material properties are key aspects for its spreading at industrial level. The conception of a robust method to produce "smart" components, whose internal structure is printed according to specific mechanical constraints and in function of the expected operating conditions, could represent a significant advance along this process.

Contents

Introduction

The term Additive Manufacturing (AM) refers to a production process which creates parts and complex geometries through the addition of material instead of through its subtraction. After about thirty years of activity this technology still records growth rates of nearly 35% [5], which underlines the extreme importance it is increasingly acquiring in the industrial manufacturing scenario. The main reasons for that can be found in the economic advantages as well as in the simpler design process [6, 7, 8]. The growing interest for its application in the production industry has pushed the research to strive for an enhancement of his products' resistance through the adoption of both new materials (passing from polymers to metals [9]) and optimized printing algorithms. The proposed study belongs to the area of the optimized printing algorithms and its purpose is the measurement and assessment of the mechanical resistance of FDM specimens that present enhanced fracture thoughness thanks to the application of a "smart" thread deposition technique. The innovating deposition criterion requires the deposited filament to follow the principal stress directions within the printed sample in order to obtain an improvement of his mechanical resistance which can lead to an increase of the maximal force at fracture up to nearly 20% [1]. The first step of the manufacturing procedure consisted in determining the stress field within a classical bending specimen using finite elements simulation. Some samples were then printed reproducing within the material structure the principal stress directions with the filament deposition. Hence the Single Edge Notched Beam (SENB) standard test procedure was executed and Digital Image Correlation (DIC) analysis was implemented in parallel to investigate the displacement fields of the specimens undergoing deformation. The present study aims to find a robust method to evaluate the obtained fracture toughness enhancement through the fitting of DIC measurement with an analytical displacement field. This analysis allowed to implement an optimization method that permits to measure the fracture toughness in condition of not pure elasticity. In fact, with the lack of a valid constitutive law of the material in presence of plasticity, it's not possible to extract the stress field from the strain and displacement fields yielded by DIC. The method consists in fitting the opening displacement field, extracted from the DIC analysis, with the analytical equations of the Williams-Westergaard (WW) model, adopting a random sampling computational method that, if properly calibrated, can potentially offer a very good approximation of the critical SIF when little plasticity is present. A Monte Carlo method was used for this purpose. Another related issue that has been tackled in the study is the definition of a reliable method to detect the onset of the crack propagation during the bending test. This datum is in fact required as preliminar information for the computation of the critical SIF value, which is representative of the material's fracture toughness. The proposed detecting technique exploits the DIC tools to locally analyze and differentiate the behavior, in terms of correlation coefficient, displacement and strain, of areas located near the notch tip or along the crack path, in order to relate the behavior's divergences with the material rupture.

This study represents an intermediate stage of a research project whose goals are both to conceive a robust method to produce "smart" components, whose internal structure is printed according to specific mechanical constraints, and to collect data in order to develop a numerical model for this purpose. The possibility of running numerical analysis of FDM products would provide an extremely useful tool for the transition from specimens to a case of study [1].

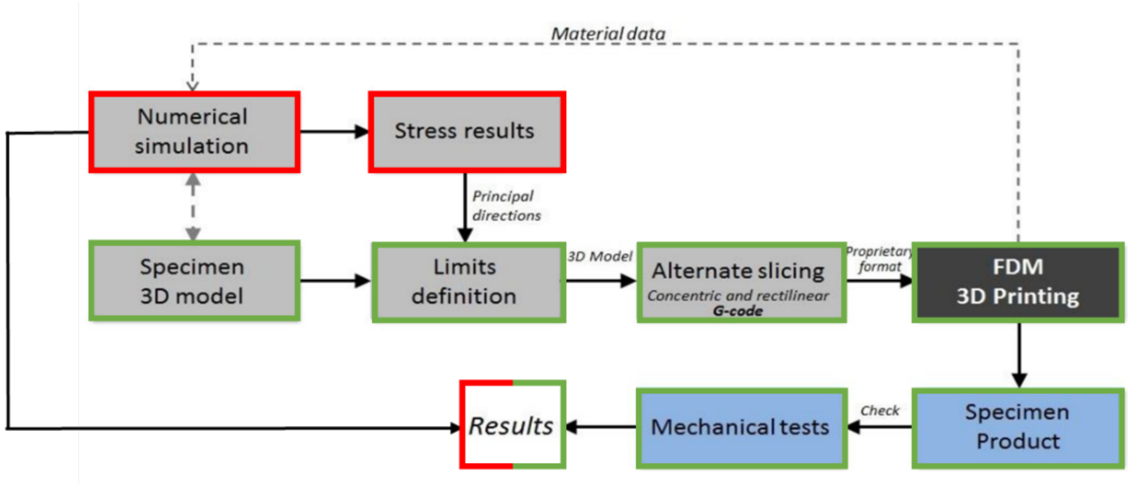

Figure 1: Global research flowchart.

Figure 1 represents the complete organisation of the global research project. As common practice the procedure is divided in two parts: experimental (in green) and numerical part (in red). The experimental part has to provide the material characteristic data as input for the numerical simulation such as the elastic modulus, the Poisson coefficient and a behaviour law of the material in the classical deposition's configuration. Furthermore, to validate the numerical model it is necessary to compare the simulation with some experimental parameters.

In the first chapters a brief overview of the technologies involved in the project and a summary of the previous phases of the study are reported in order to better collocate this work within the global outlook. The interested parts of fracture mechanics are introduced too.

Bibliography

Technologies

Fused Deposition Modeling

Depending on the material and its hardening system [6] various AM technologies have been developed. Among them there are the extrusion technologies, in which is included the Fused Deposition Modeling (FDM): a process that, through the extrusion of a fused thermoplastic filament from a heated nozzle, builds tridimensional objects layer by layer. While FDM is one of the most used additive manufacturing techniques today, due to its ability to manufacture very complex geometries, the major research issues have been to balance ability to produce aesthetically appealing products with functionality. The reduction of product development's cycle time is a major concern in industries to remain competitive in the marketplace. Several sources have highlighted the advantages of additive manufacturing techniques over traditional product development methodology. Using AM speeds up the whole product development process especially when producing very complicated parts which may be challenging using traditional manufacturing methods: regardless of the complexity of parts to be built, building with an AM machine is generally performed in a single step unlike in most other manufacturing processes which normally require multiple and iterative stages to be carried out. In addition to these advantages, other benefits of using AM are the significant reduction in the number of processes and resources required. Producing aesthetically appealing AM products that have complex shapes is not difficult. The challenge is to produce parts that are functionally reliable. Despite several design and environmental advantages of AM technologies over other manufacturing processes, full scale application has not gained much attention yet because of compatibility issues of currently available materials with AM technologies. There are possibilities to use some metals (such as steel alloys and titanium) and ceramics, but the majority of materials used by modern AM applications are polymers. The material properties are typically not as strong as their conventionally manufactured counterparts, due to the anisotropy caused by the layered structure and to the weakness of the welding lines. To overcome this limitation, one approach may be the development of new materials having superior characteristics than the conventional materials used today. Another convenient approach may be to suitably adjust the process parameters during the fabrication stage so that the resistance properties may improve. The properties of AM parts are in fact function of various process related parameters and can be significantly improved with a proper adjustment. Since the mechanical properties are of utmost importance for functional parts, it is absolutely essential to study the influence that these parameters have on them.

Process

The FDM process begins with a 3D CAD model which is then saved into a STL format file. Hence a specific AM software cuts the piece model in slices in order to get a new file containing information for each separate layer and finally a G-code type language is required to transform the slicing in the trajectories that the extruder will follow. The technology is similar to a three axes numerical control machine and, while originally it used a G-code language, lately manufacturers converted it into proprietary formats for their machines. The build material is initially in the raw form of a flexible filament. The feedstock filament is then partially melted and extruded though a heated nozzle within a temperature controlled environment for building of the part. The material is extruded in a thin layer onto the previously built layer and, when deposited it cools, solidifies, and bonds with adjoining material. After an entire layer is deposited, the build platform moves downward by an increment equal to the filament height (layer thickness) and the next layer is deposited on top of it (Fig.3). The deposition trajectory is defined to fill the piece and usually to create a shell made of 45° tilted stripes between alternate layers. The most commonly used materials in FDM are Acrylonitrile Butadiene Styrene (ABS), Poly-Lactic Acid (PLA), and Poly-Carbonate (PC). Being deposited close to each other on the same plane, the warm threads weld together and the same happens between the layers. The support material is often made of another material and is removable or soluble from the actual part at the end of the manufacturing process (except for the low cost solutions, which use the same). In order to predict the mechanical behavior of FDM printed parts it's essential to comprehend before the properties of the raw material in that specific structural configuration and to know how the printing parameters influence the resulting material features[10].

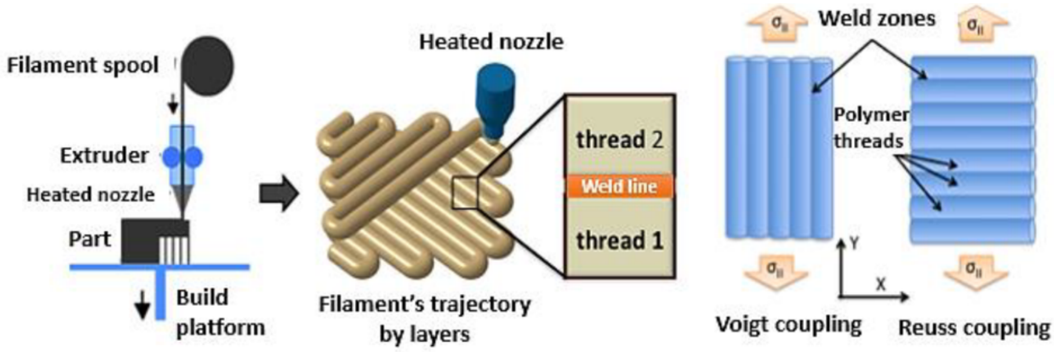

Figure 2: (a) Working principle of FDM and a classical trajectory deposition. (b) Weak and strong filaments coupling with respect to the stress direction.

Research and Development

Among the several AM techniques, FDM presents some positives characteristics: the programming simplicity, a quite large variety of usable materials and a low cost. However, the accuracy and the surface quality are lower if compared to other typologies. For this reason the optimization proposed by Gardan et al.[1], together with surface finish improving techniques[11, 12, 13, 14], represent an interesting development. The determination of quality influential parameters has been tackled in many researches [15, 16] and most of them used a classical layered structure and mechanical tests through a design of experiment approach. From the literature, it is found that good amount of work has been done in FDM strength modelling; however, little amount of work has been done to develop the strength model in terms of FDM process parameters for prediction purpose. Several researchers have specifically considered the anisotropic characteristics of FDM parts in recent years. Rodríguez et al.[17] investigated the tensile strength and elastic modulus of FDM specimens with varying mesostructures in comparison with the properties of the ABS monofilament feedstock. The outcome of their investigation is that the tensile strength was the greatest for parts with fibers aligned with the axis of the tension force. Ahn et al.[18] determined that both air gap and raster orientation had significant effects on the resulting tensile strength, while compressive strength was not affected by these factors. Onwubolu et al.[19] investigated five important process parameters such as layer thickness, part orientation, raster angle, raster width, and air gap. Minimum layer thickness improves tensile strength, although is more costly due to more material usage for manufacturing parts. Part orientation plays a major role: for zero part orientation (with the part orientation coinciding with the direction of tensile loading), maximum tensile strength is obtained. Raster angle has the tendency to affect the internal structure of the finished product. Each neighbouring layer has a raster angle perpendicular to the immediate preceding layer. The raster width is known to affect the finished AM part in such a way that the larger the raster angle the greater the tendency for the finished part to withstand higher tensile stress. Negative air gap produces finished AM part that withstand higher tensile stress. J.Li et al.[20] enhanced the fracture toughness of single edge notch tension (SENT) specimens by modifying the surface topology by adding small cylinders on both top and bottom surfaces. The added pattern on the surface act as obstacles for the crack to initiate as well as during propagation and it increased the initial fracture toughness and strain energy release rates for all sample types. Other studies on the printer settings (ex. layer thickness, air gap, raster angle and so on) have also been carried out to increase the mechanical strength [21]. The layer thickness is confirmed to be one of the most influencing parameters. In particular, has already been shown in a research that increasing the layer thickness reduces the mechanical strength [19]. However, another remark about thinner layers is the increase in fabrication time, therefore it's necessary to evaluate to what extent increasing the printing time worths the resistance increase.

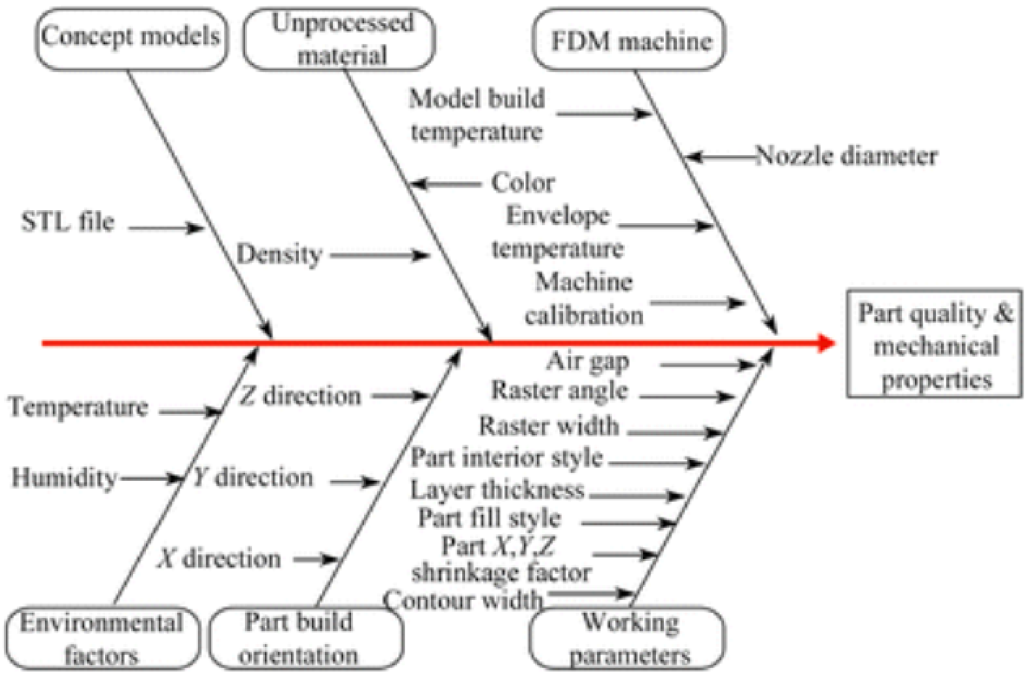

Figure 3: FDM process and influencing parameters.

About the internal structures of 3D printed products some studies, like [22], investigated the use of lattice structures including rapid prototyping to lighten sandwich panels while maintaining their mechanical strength. The study determined that the directions of the anisotropy of the lattice influences the mechanical behavior of the entire panel. Other studies developed specific structures like curved [26], honeycomb [23] or cell shapes, “tetrachirales” [3] or “hexachirales” [25]. These structures suggest a global infill of product without considering the localized mechanical stresses. Currently, topological optimization can be used to change the inner structure of a printed shape in order to enhance the mechanical strength [6, 24]. In such a case, the geometry is suggested assuming that the material is isotropic without taking into account the layered structure of the material obtained by FDM. Orienting the thread deposition to reproduce a structure suited to mechanical constraints is a new track to explore.

The goal is to find an alternative to honeycomb or cell shapes structures, currently suggested as standard by FDM 3D printers. The present experimentation required quite thick specimens (10 mm) to avoid instabilities during bending as observed during the preliminary tests. The layer chosen thickness has been 0.25 mm for coherence with previous researches [2]. However, such a thin layer made the first layer filling very difficult so it was decided, in order to grant better adherence of the piece to the building plate, to print a 0.35 mm thick first layer. The autors chose ABS as material and used a Makerbot Replicator 3D printer (Fig.2) to manufacture the specimens.

Figure 4: FDM printer used in this work: Makerbot Replicator.

Digital Image Correlation

Experimental techniques such as thermoelasticity and photoelasticity have been successfully used to characterise the elastic stress fields around cracks but they do not take into account either plasticity or anisotropy[27]. Considerable work has been carried out to characterize crack tip stress fields from displacement measurements. The currently most common method adopted to obtain displacement field data is DIC. It is an non-contact optical technique that provides full field displacement information and that has found application in evaluating fracture parameters for both linear elastic fracture mechanics (LEFM) and elastic plastic fracture mechanics (EPFM) problems [28]. DIC permits to compute the displacement field within a "Region Of Interest" (ROI) for a material sample undergoing deformation [29, 30, 31]. This is obtained tracking the deformation of the object through a series of photo taken in successive moments. A digital image is essentially a two-dimensional array of intensity values which can be discretized into small subsets, which are properly spaced groups of pixels. Image correlation works by matching the small square subsets of an undeformed image to locations in the image of the surface after deformation, as illustrated in Fig.5, by means of a series of mathematical mapping and cross correlation functions. The comparison is possible thanks to random speckled pattern which gives a non-uniform local average level of grey. To recognize this pattern mathematically, the intensity of each pixel in the reference and deformed images can be traced and the displacement vector can be determined. However, it would be extremely difficult to distinguish every single pixel on the image and therefore at least 3x3 pixels are needed for one recognizable feature [27]. The ideal subset size should contain at least three clear features but it is often a compromise between resolution and accuracy. As a general rule, larger subset sizes will increase the accuracy whereas a smaller subset will increase the resolution but realistically the size of a subset is determined by the quality of the image and speckle pattern [27].

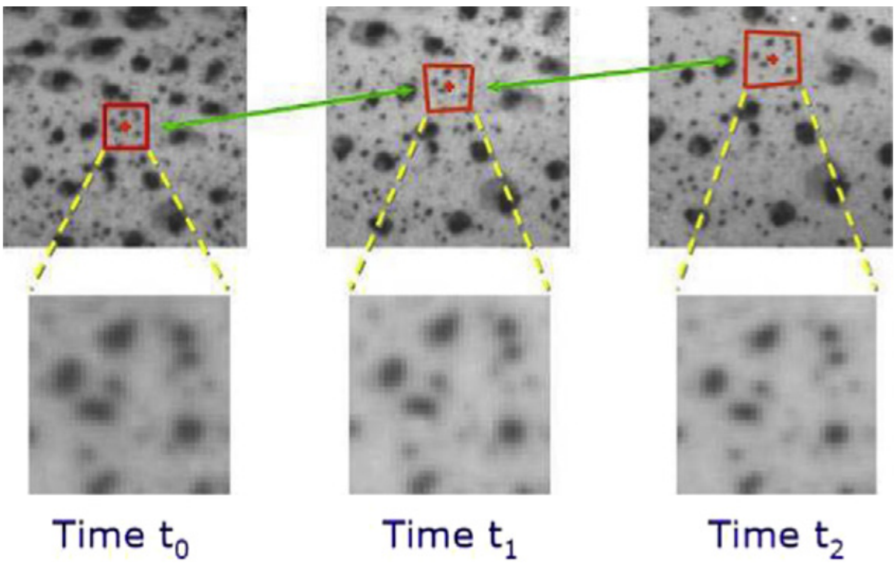

Figure 5: Matching reference subset and current subset [27].

A variety of methods can be used to produce a random pattern on the surface. Sometimes the natural pattern of the material is enough to produce a suitable pattern. Glass or emery paper can be used to scratch the surface of the specimen to generate a random pattern. More conventionally, the random pattern is produced by spray painting the surface or using dry toner with an adhesive medium. These techniques normally suffice for macro DIC applications but for micro scale more care is needed when producing the random pattern due to the speckle size and it often requires the use of an airbrush or lithography [27]. Fig.6 illustrates the typical set-up of a 2D DIC. A 3D system will have two cameras at different angles to obtain a 3D perspective of the specimen surface.

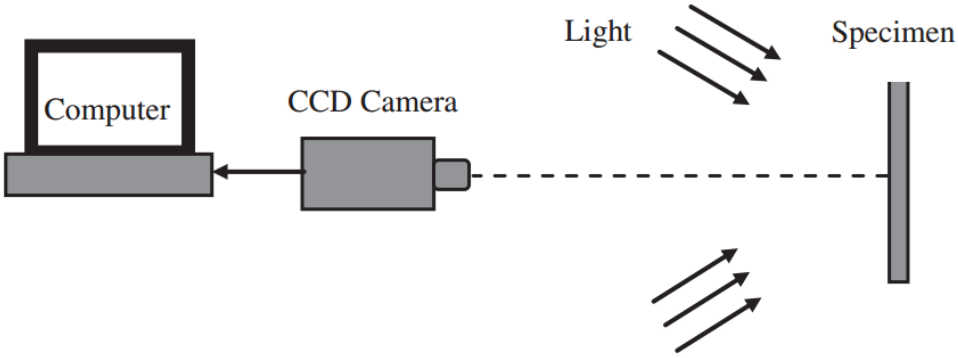

Figure 6: Schematic diagram of typical 2D DIC equipment [27].

Using the first order Taylor series the approximated displacement fields can be identified as:

$$x_{cur,i} = x_{ref,i} + u_{rc} + \frac{\partial u}{\partial x_{rc}} \cdot (x_{ref,i} - x_{ref,c}) + \frac{\partial u}{\partial y_{rc}} \cdot (y_{ref,j} - y_{ref,c}) \tag{1}$$

$$y_{cur,j} = y_{ref,j} + v_{rc} + \frac{\partial v}{\partial x_{rc}} \cdot (x_{ref,i} - x_{ref,c}) + \frac{\partial v}{\partial y_{rc}} \cdot (y_{ref,j} - y_{ref,c}) \tag{2}$$

With:

- $(x_{cur,i}, y_{cur,j})$: coordinates of the final subset point.
- $(x_{ref,i}, y_{ref,j})$: coordinates of the initial reference subset point.
- $(x_{ref,c}, y_{ref,c})$: coordinates of the initial centre of the reference subset point.

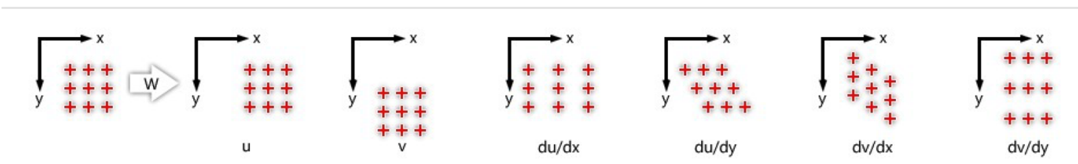

Figure 7: Representation of all the possible components of the displacement field [27].

This process is automatized through an iterative nonlinear least squares optimization scheme. Once solved it, it is possible to obtain the displacement field and to properly store it into a matrix. Knowing the displacement field it is then possible to pass to the strain field. The Green-Lagrange strain has been computed in this case by using the resulting plane slopes as follows:

$$\epsilon_{xx} = \frac{1}{2}\left(2\frac{\partial U}{\partial x} + \left(\frac{\partial U}{\partial x}\right)^2 + \left(\frac{\partial V}{\partial x}\right)^2\right) \tag{3}$$

$$\epsilon_{yy} = \frac{1}{2}\left(2\frac{\partial V}{\partial y} + \left(\frac{\partial U}{\partial y}\right)^2 + \left(\frac{\partial V}{\partial y}\right)^2\right) \tag{4}$$

$$\epsilon_{xy} = \frac{1}{2}\left(\frac{\partial U}{\partial y} + \frac{\partial V}{\partial x} + \frac{\partial U}{\partial x}\frac{\partial U}{\partial y} + \frac{\partial V}{\partial x}\frac{\partial V}{\partial y}\right) \tag{5}$$

The gradients can be obtained through the IC-GN method. This method is used to solve non-linear least squares problems and it is a modification of Newton's method for finding a minimum of a function [2]. However, to reduce the noise and have better results, the strain field is instead obtained with a surface fitting (Fig.8). This fitting can be set during the analysis and regulated with the strain radius (smaller radius results in better fit and higher precision).

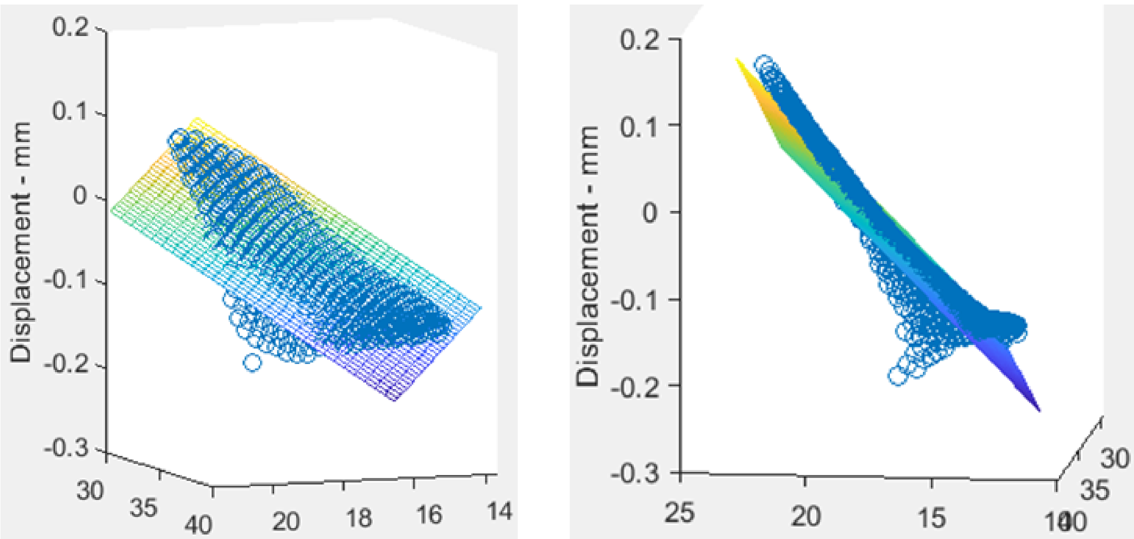

Figure 8: Surface fitting to obtain the strain field during the DIC analysis.

In any experiment, out-of-plane motions are unavoidable. This can be due to factors such as Poisson's effect, deviations from planarity, small amounts of specimen bending, and deviations from ideal grip constraints. DIC is relatively simple to use and allows the direct experimental and numerical computation of fracture parameters such as the crack mouth opening displacement, energy release rate and stress intensity factors.

Fracture Toughness

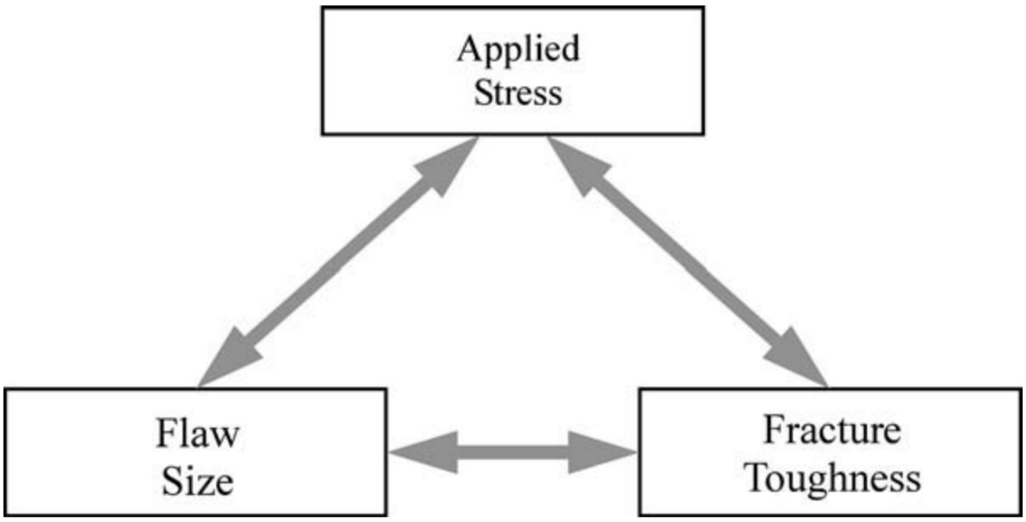

Figure 9: Fracture mechanics quantifies the critical combinations of these three variables.

When we are in presence of a singularity or a flaw there is a small region of plastic deformation around the tip in which the material becomes harder. If the plastic zone is very small LEFM is applicable, otherwise EPFM is necessary. The reference parameters to assess the fracture toughness of a material in LEFM are the energy release rate and the stress intensity factor, the parameters for EPFM are J-integral and COD/CTOD. In the present work it has been made the assumption of linear elastic behavior, hence the energy release rate and the stress intensity factor have been investigated.

There are two alternative approaches to fracture analysis: the energy criterion and the stress intensity approach. These two approaches are equivalent in certain circumstances [32]. Either were attempted in different steps of this work. At the end, the stress intensity approach was applied because it yielded more robust and reliable results and because the energy approach would have required an accurate measurement of the crack lenght, which was not an easy task.

Effect of Material Properties

Figure 10 is a schematic plot of failure stress vs. fracture toughness K_{Ic}. For low toughness materials, brittle fracture is the governing failure mechanism, and critical stress varies linearly with K_{Ic}. At very high toughness values, LEFM is no longer valid, and failure is governed by the flow properties of the material. At intermediate toughness levels, there is a transition between brittle fracture under linear elastic conditions and ductile overload. Nonlinear fracture mechanics bridges the gap between LEFM and collapse. If toughness is low, LEFM is applicable to the problem, but if toughness is sufficiently high, fracture mechanics ceases to be relevant to the problem because failure stress is insensitive to toughness; a simple limit load analysis is all that is required to predict failure stress in a material with very high fracture toughness. In this work it was assumed to have small plastic deformation and therefore the LEFM was applied.

The typical layered structure of the products of FDM plays an important role in the resulting fracture behavior of the examined specimens. A crack in a material with strongly orthotropic fracture properties, or a crack in an interface with a fracture toughness that is distinct from the materials joined across it, can experience either kinking or straight-ahead propagation under mixed mode loading depending on a number of factors, including the relative toughness associated with the competing directions of advance [33]. If an interface is a low-toughness fracture path through joined solids, then one must be concerned with mixed mode crack propagation since the crack is not free to evolve with pure mode 1 stressing at its tip, as it would in an isotropic brittle solid. The asymmetry in the moduli with respect to the interface induces a mode 2 component [33]. The competition between crack advance within the interface and kinking out of the interface depends on the relative toughness of the interface to that of the adjoining material. In mixed-mode conditions a crack changes its growth direction when subjected to mixed mode loadings. In practice, cracks follow the path of the lowest material resistance or weakest material orientation arising from process history, composite reinforcement, or interfaces as in the present case.

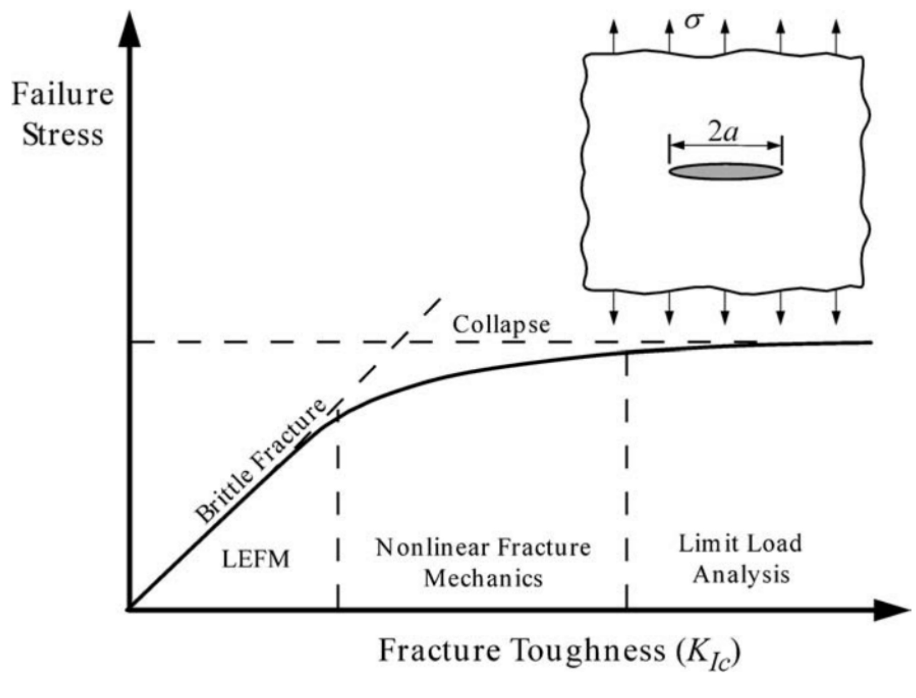

Figure 10: Effect of fracture toughness on the governing failure mechanism.

Energy Approach

According to the first law of thermodynamics, when a system goes from a non-equilibrium state to equilibrium, there is a net decrease in energy. Griffith applied this idea to develop a fracture theory based on energy rather than local stress. A crack can form (or an existing crack can grow) only if such a process causes the total energy to decrease or remain constant. Thus the critical conditions for fracture can be defined as the point where crack growth occurs under equilibrium conditions, with no net change in total energy. In order for this crack to increase in size, sufficient potential energy must be available in the plate to overcome the surface energy of the material. The Griffith energy balance for an incremental increase in the crack area dA, under equilibrium conditions, can be expressed in the following way:

$$\frac{dE}{dA} = \frac{d\Pi}{dA} + \frac{dW_s}{dA} = 0 \tag{6}$$

where E is the total energy, Π is the potential energy supplied by the internal strain energy and external forces and W_s is the work required to create new surfaces. The Griffith model is based on a global energy balance: for fracture to occur, the energy stored in the structure must be sufficient to overcome the surface energy of the material.

Energy Release Rate

The energy approach states that crack extension (i.e., fracture) occurs when the energy available for crack growth is sufficient to overcome the resistance of the material. The material resistance may include the surface energy, plastic work, or other types of energy dissipation associated with a propagating crack. Griffith was the first to propose the energy criterion for fracture, but Irwin is primarily responsible for developing the present version of this approach: the energy release rate G, which is defined as the rate of change in potential energy with the crack area for a linear elastic material:

$$G = -\frac{d\Pi}{dA} \tag{7}$$

Since G is obtained from the derivative of a potential, it is also called the crack extension force or the crack driving force. Crack extension occurs when G reaches a critical value, i.e.:

$$G_c = \frac{dW_s}{dA} = 2w_f \tag{8}$$

where G_c is a measure of the fracture toughness of the material.

The potential energy of an elastic body, Π, is defined as follows:

$$\Pi = U - F \tag{9}$$

where U is the strain energy stored in the body and F is the work done by external forces.

The strain energy change with the crack growth for constant displacement is $\Delta U = 0.5vdP$. In this experiment the mechanical tests have been carried out with a constant displacement rate. Consider a cracked plate that is loaded at fixed displacement, as illustrated in Figure 11. When displacement is fixed, the plate is displacement controlled and the strain energy decreases; $F = 0$ and $\Pi = U$. Thus:

$$G = -\frac{1}{B}(\frac{dU}{da})_{\Delta} = -\frac{\Delta}{2B}(\frac{dP}{da})_{\Delta} \tag{10}$$

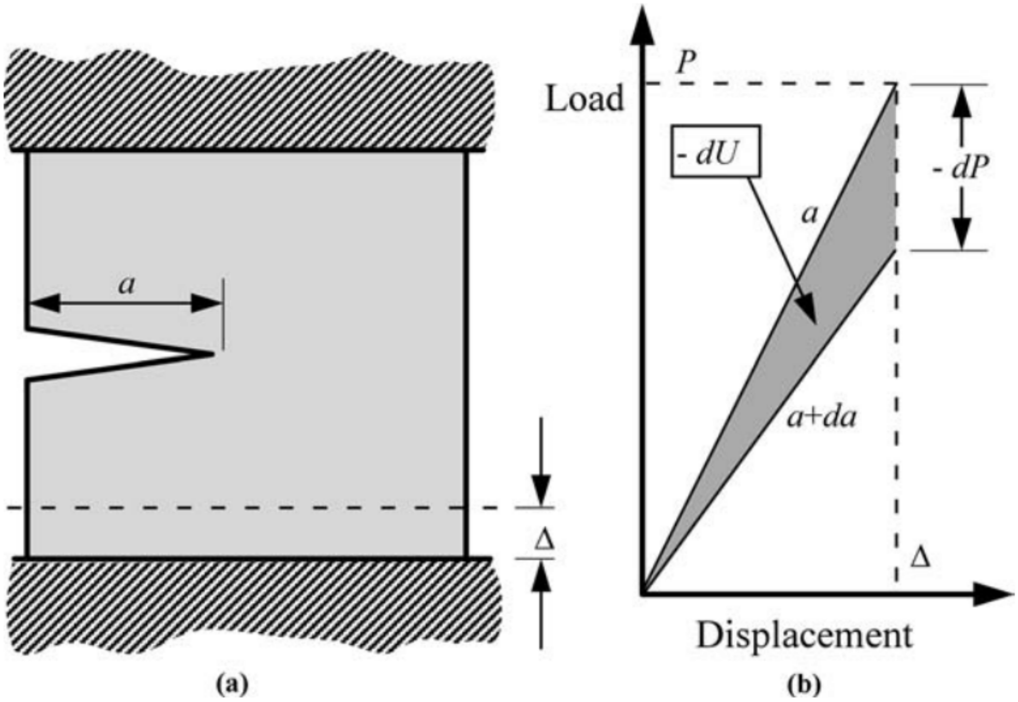

Figure 11: Cracked plate at a fixed displacement Δ.

Stress Intensity Approach

The theoretical cohesive strength of a material is approximately E/π, but experimental fracture strengths for brittle materials are typically three or four orders of magnitude below this value. The discrepancy between the actual strengths of brittle materials and theoretical estimates is due to flaws in these materials. Fracture cannot occur unless the stress at the atomic level exceeds the cohesive strength of the material. Thus, the flaws must lower the global strength by magnifying the stress locally. The ratio between the theoretical critical stress and the actual critical stress is defined as the stress concentration factor k_t.

Figure 12 shows a square element near the tip of a crack in an elastic material in a mode I (tensile) loading case, together with the in-plane stresses on this element. Each stress component is, in these operating conditions, proportional to a single constant K_I. If this constant is known, the entire stress distribution at the crack tip can be computed with the equations reported in the same figure. Such constant, which is called Stress Intensity Factor (SIF), completely characterizes the crack tip conditions in a linear elastic material. If one assumes that the material fails locally at some critical combination of stress and strain, then it follows that fracture must occur at a critical stress intensity K_{Ic}. Thus, K_{Ic} is an alternative measure of fracture toughness.

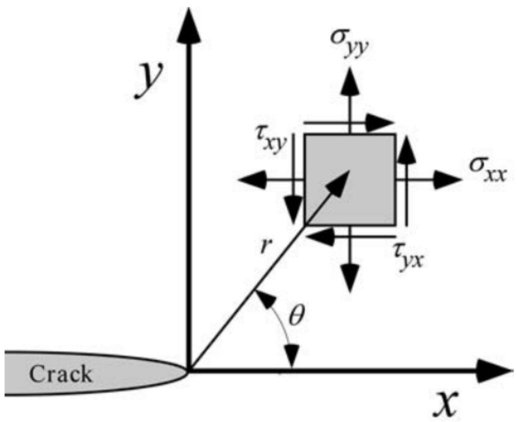

$$\sigma_{xx} = \frac{K_I}{\sqrt{2\pi r}} \cos\left(\frac{\theta}{2}\right)\left[1 - \sin\left(\frac{\theta}{2}\right)\sin\left(\frac{3\theta}{2}\right)\right]$$

$$\sigma_{yy} = \frac{K_I}{\sqrt{2\pi r}} \cos\left(\frac{\theta}{2}\right)\left[1 + \sin\left(\frac{\theta}{2}\right)\sin\left(\frac{3\theta}{2}\right)\right]$$

$$\tau_{xy} = \frac{K_I}{\sqrt{2\pi r}} \cos\left(\frac{\theta}{2}\right)\sin\left(\frac{\theta}{2}\right)\cos\left(\frac{3\theta}{2}\right)$$

Figure 12: Stress field near the crack tip in an elastic material in a mode I (tensile) loading case.

Failure occurs when $K_I = K_{Ic}$. In this case, K_I is the driving force for fracture and K_{Ic} is a measure of material resistance. The relationship between K_I and G is:

$$G = \frac{K_I^2}{E} \tag{11}$$

The same is obviously valid for G_c and K_{Ic}. Thus, the energy and stress-intensity approaches to fracture mechanics are essentially equivalent for linear elastic materials.

Previous Work

Smart Deposition

As already said, the aim of the research is to print a specimen using the thread deposition more suited to the mechanical constraints of the product according to its use. As it is known, in mechanics it is possible, given any stress state, to identify a referent frame for which stress tensor is diagonal. These stresses are called principal stresses (σ_1, σ_2 and σ_3 for a 3D stress state). It is sufficient to place the filament in directions of these stresses in order to gain a greater resistance to fracture. It has been supposed to be in the case of an elastic-plastic material (under small scale yielding conditions[1]), the ABS, loaded under tensile mode. For testing a method similar to the one of Tohgo et al.[3] has been used, which includes three points and four points bending tests. In addition to these tests, some tensile tests have been run to characterize the material for future application in numerical modelling. In all tests Digital Image correlation was used.
The FDM process leads to an heterogeneous structure because of the presence of welding lines, which are weaker, between the filaments. In commonly used printers, these trajectories are predefined and not based on specific mechanical constraints. As a consequence the welding lines can be found oriented inconveniently, resulting in a reduction of the mechanical strength. To avoid this problem, the main tensile stresses within the structure must be held by the filaments, not by the welding lines. In order to fulfill this condition the filament must be tangent to the principal stress directions when the principal stresses are mainly tensile. As a result the force lines in the material will be guided by the filaments. Since two principal directions exist, both of them have been taken into account and filament deposition has subsequently been performed according to each direction.

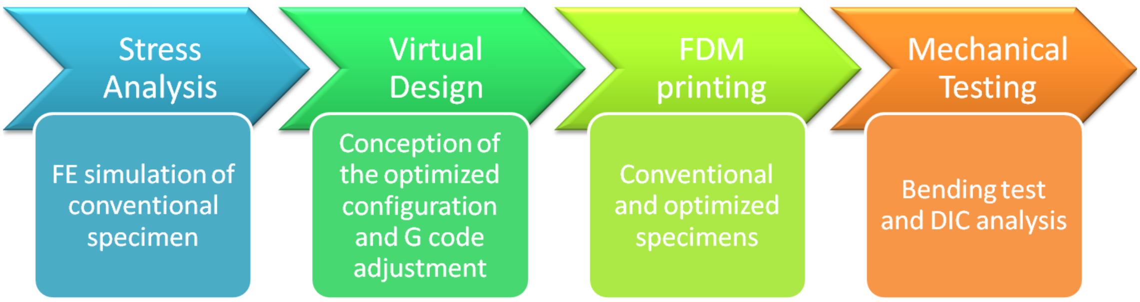

Figure 13: The various steps of the preliminary stage of the research project.

[1]Since the yelding is small we can assume a behavior simile elastic and use the LEFM.

Stress-based Criterion

Finite elements (FE) simulation of an homogeneus, linear elastic model has been used to compute the principal stresses and strains in a plane stress assumption. The principal stresses σ_I and σ_{II}, which are the eigenvalues of the stress tensor, can be written as:

$$\sigma_I = \frac{\sigma_{11} + \sigma_{22}}{2} + \sqrt{\left(\frac{\sigma_{11} - \sigma_{22}}{2}\right)^2 + \sigma_{12}^2} \tag{12}$$

$$\sigma_{II} = \frac{\sigma_{11} + \sigma_{22}}{2} - \sqrt{\left(\frac{\sigma_{11} - \sigma_{22}}{2}\right)^2 + \sigma_{12}^2} \tag{13}$$

where σ_{ij} are the components of the stress tensor.

The principal directions, which are the eigenvectors of the stress tensor, can be described by the angle α and $\pi/2 + \alpha$ where:

$$\tan(2\alpha) = \frac{2\sigma_{12}}{\sigma_{11} - \sigma_{22}} \tag{14}$$

The specimens printed and used for the fracture toughness characterization are similar to standard Single Edge Notched Bend (SENB) samples. The thickness is about 10.1 mm, thus plane stress assumption is almost satisfied. The principal directions are computed at each point in the sample and have to be tangent to the printing trajectory. Since the in-plane stress is biaxial, there are two principal directions in the sample. As a consequence, two trajectories have to be taken into account in the printing. Hence, for two subsequent layers, the first (second) principal direction is used to calculate the trajectory in the first (second) layer.

Enhanced Domain

As already said, to improve the mechanical resistance of a printed sample the polymer threads must be oriented toward the tensile force field. This idea is inspired by the reinforcement principle of the composite materials where the fibers are oriented toward the in-plane tensile stress. Subsequently the geometry of the model has been split in two domains:

- The stress concentration zone around the notch tip.
- The rest of the sample where the stress magnitude is not significantly high.

The stress concentration zone is the most critical region within the sample because of the high stress level. This is the region that has to be printed carefully in order to avoid the weak configuration of threads. According to the optimized strategy of thread deposition, a mechanical resistance improvement is expected when the principal stresses are mainly tensile (both σ_I and σ_{II} are positive). This condition allows us to easily define the region where a modification of deposition trajectory would be beneficial. This “affected region” is called Ω_1 and is defined as follows:

If Ω is the entire geometry of the sample cross section and M is a random point inside it:

$$\Omega = \Omega_1 \cup \Omega_2 \tag{15}$$

$$\forall M \in \Omega \; if \; \begin{cases} (\sigma_I > 0) \;\&\; (\sigma_{II} > 0) \rightarrow & M \in \Omega_1 \\ else \;\rightarrow & M \in \Omega_2 \end{cases} \tag{16}$$

The optimization of the deposition trajectories has been performed only within the Ω_1 region.

G-code

In this work, the filament trajectory reproduces the principal stress directions, revealed by finite element simulation, within bending specimens similar to SENB samples. For this purpose a G-Code type language has been used. The 3D model used for the numerical simulation is modified to specify the limit of principal directions according to the stress fields. The model slicing is realized with open source softwares (Slic3r v 1.2.6 and Replicator G) but the G-code and the alternate layers reproducing the stress fields are processed manually into the programming language. Finally, the samples are manufactured by FDM 3D printing.

Specimens' Printing

The slicing of 3D Model (file in *.stl format) is applied with concentric fill pattern around the delimited zone according to the stress criterion. The printing trajectory must correspond to the principal directions in the delimited zone. The other domain is less stressed (in the tensile direction) and is printed with non-respect to the principal direction conditions. The G-code is modified to alternate the layers with the principal directions and the less stressed direction. Two types of bending samples are printed. The first "classical" sample is got by linear infilling with 45 degree depositing by alternate layers and the second "optimized" sample uses the optimized generative trajectory method.

Slic3r

The global geometry and the specific geometry were imported as different objects on Slic3r and then they were manually assembled. This was done for both layer I and layer II. Finally, in the gcode of layer I was manually substituted the gcode of layer II obtaining an alternation of layer I and layer II. However, thanks to the option "*modifier*" given by Slic3r it has been possible to increase the degree of automatization and personalization of the printing. Indeed, using this feature it is possible to change the printing parameters for each determined sub volume. It has been necessary to adopt either rectilinear or concentric filling direction, since it is demanded a 100% infill with a regular pattern. It is possible to obtain better sketches importing the simulation photo, properly scaled, directly on the CAD modeller.

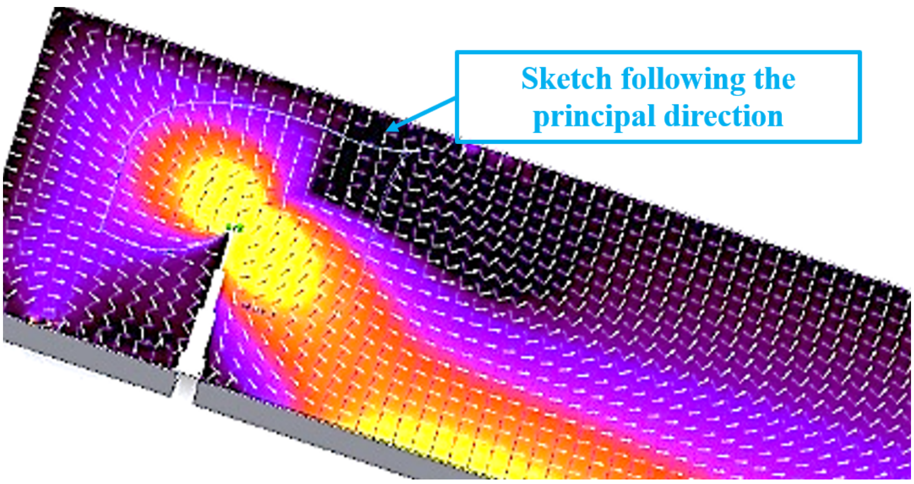

Figure 14: Most solicited zone profile on the FEM simulation photo imported on Solidworks.

But a better geometric modelling of the most affected area is not the only possible improvement with this passage. In fact, it would be interesting to keep optimizing the process defining a boundary of the most affected area corresponding to the best built time/resistance gain ratio. To study the radius of effectiveness of the optimized thread deposition would result in a reduction of time in favour of the same or a similar optimisation. Indeed, there is a strong probability that the areas modified in these tests are larger than those needed to achieve the desired optimisation. A possible criterion might be identified with a ratio of stresses α, for example $\sigma_{max} \cdot \alpha = \sigma_{lim}$ where σ_{lim} is the stress on the border of the new optimized most affected zone.

Parameter	Value
First Layer Thickness	*0.35 mm*
Layer Thickness	*0.25 mm*
Brim Width	*5 mm*
Speed Solid Infill	*80 mm/s*
Perimeters Speed	*60 mm/s*
First Layer Speed	*30 mm/s*
Bed Temperature	*120°C*
Extruder Temperature	*235°C*
Gcode Flavour	*MakerWare*

Table 1: Slic3r (v1.2.9) printing parameters.

Specimen A

In the present section is reported the bending specimen chosen according to Thogo and Ishii's work[3]. In the particular configuration used the specimen is loaded under pure mode I and it is similar to a SENB (Fig.9). Regarding the thickness, it has been kept into consideration that if the specimen is too thin, during the bending test it can show instabilities along the z axis (throughout the thickness). A 10mm thickness has been chosen for all the specimens[2]. An increase in built time was expected, since it is printed a more complicated pattern than a concentric filling.

	Classic	Optimized	Comparison
Built Time	2h 26min	2h 46min	**+13.3%**
Material (mm)	30928	30984	**+0.2%**

Table 2: Printing data.

[2]The actual thickness is 10.1mm because of the necessity of a thicker first layer (0.35mm) for better adhesion.

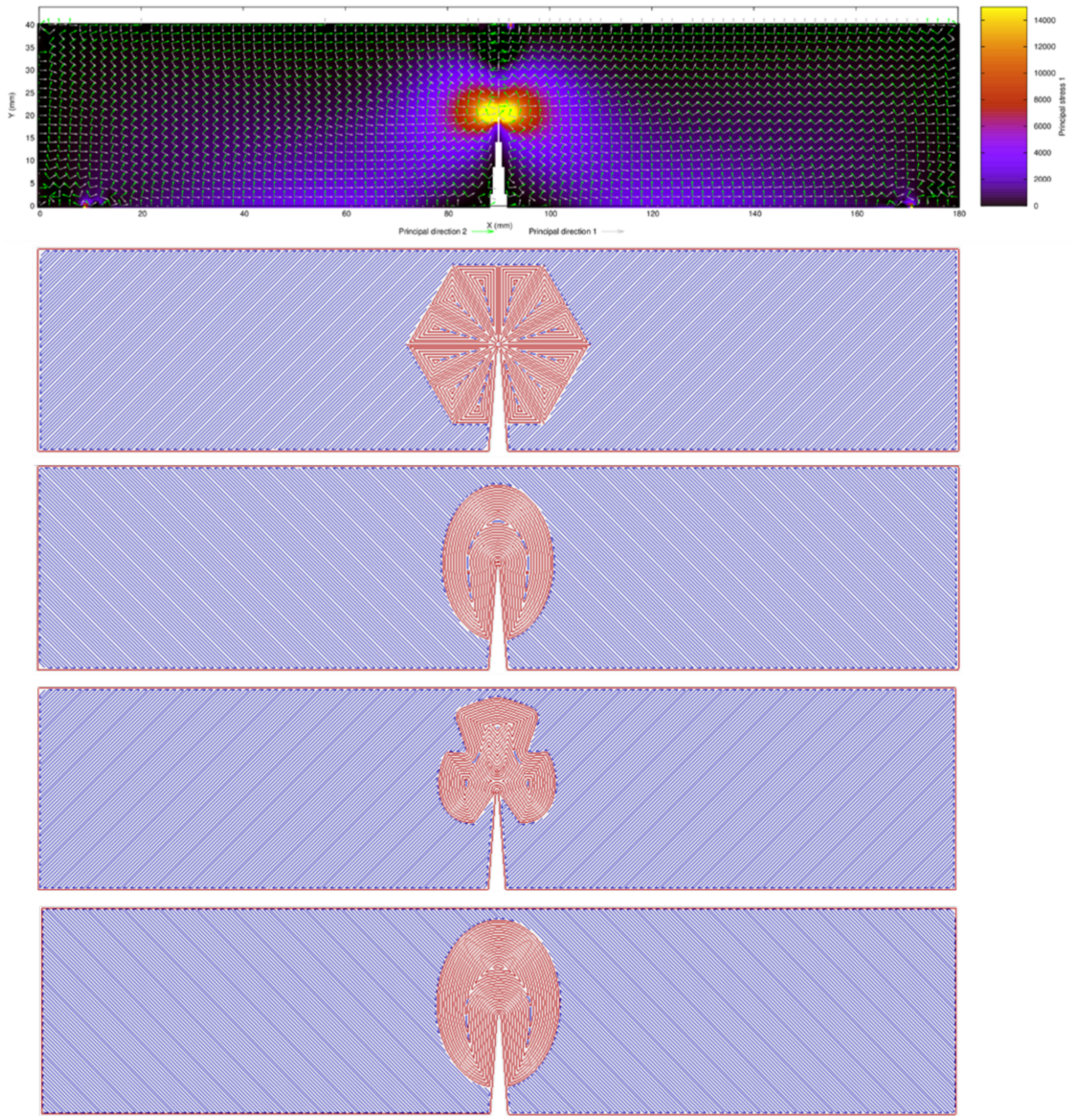

Figure 15: **FE simulation of an optimized specimen: configuration A**. From top to bottom: layer 1 σ_1 version 1, layer 2 σ_2 version 1, layer 1 σ_1 version 2 and layer 2 σ_2 version 2

Mechanical Test

Tensile Test

To provide the material's experimental data and to build the numerical model to predict the fracture behaviour, a tensile test has been preliminarily carried out. In order to obtain the data to give as input to the numerical simulation the Elastic modulus, the Poisson's ratio, the tensile strength and a characteristic equation from the data fitting are demanded. To obtain all the informations needed for the numerical model the test of three different configurations was required: the chosen raster angles are 0°, 45° and 90° and three specimens for each kind have been printed and tested. The aim was to define the properties of both threads and weldings.
The test is equal to a classic tensile test with imposed strain rate adding a photo shoot every defined time gap. Defining this time gap is highly important because it determines the number of points that it can use to build the material characteristic curve. After having chosen the deformation speed imposed by the machine ($V_m = 1\,\mathrm{mm/min}$) and the number of pictures in a defined interval (20 between 0 and 0,15mm of displacement[3]) it is possible to define the time as follows:

$$t_{gap} = \frac{\Delta l \cdot 60}{V_m \cdot N_{photo}} = 0.45\,\mathrm{s} \cong 0.5\,\mathrm{s}$$

With the deformation curve given by the machine it is possible to discern the force applied at the determined instant every photo has been taken. Hence, simultaneously at each photo shoot a point on the tensile curve was registered by the traction machine. The experiment was run on a $5kN$ tensile machine (Instron 4411). The software handling the machine was Version Series IX 8.06.00 with a load cell of $50N$ since it was expected maximum $1kN$ of force applied. The camera used was a SONY SPT-M308CE and the acquisition of the photos was handled through the software Image Plus. The resulting photos (768x576 pixels) in 16 levels of grey had a resolution of 100x100 dpi. Among the different typologies and colours of paint used better results have been obtained with matt, high covering and rapid dry paints. The advantages are both in preparation time and image quality.
For the 45° configuration it would be expected a tensile strength value between the longitudinal and the horizontal. This because the longitudinal measure the resistance of fibres (highest), the horizontal the resistance of the surface interface (lowest) and the 45° their cooperation. It's interesting the ideal plastic flow behaviour present in the 45° configuration (Fig.17). A "comeback" to the end of the curve can be observed (Fig.16). A first

[3]The target was to have between 10-15 pictures in the elastic trait.

hypothesis is that this is connected to the propagation of the fracture in the tensile specimens. Indeed, this caused the debonding phenomenon and the reduction of the resistant section.

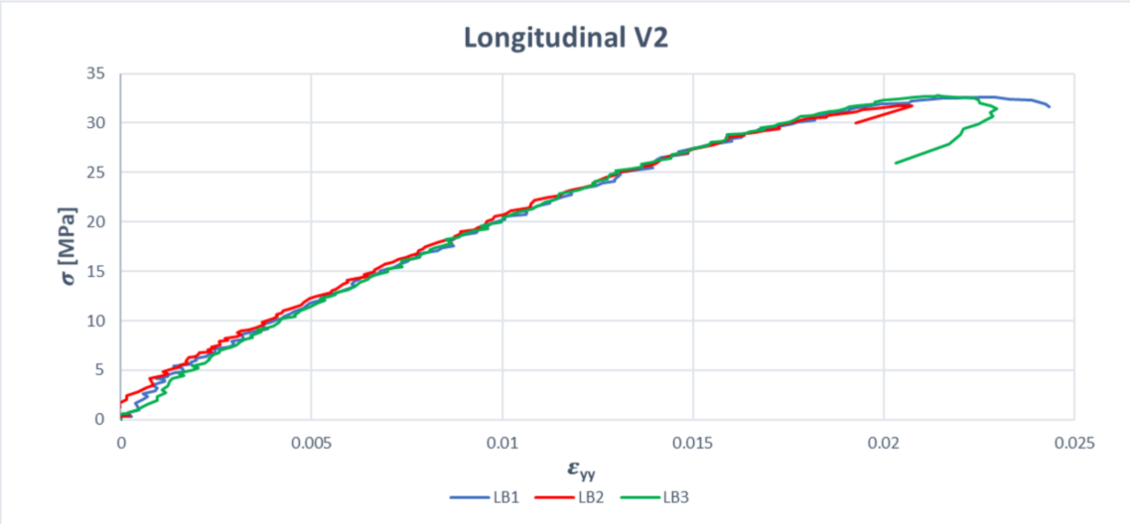

Figure 16: Tensile Test of specimens with longitudinal filament deposition.

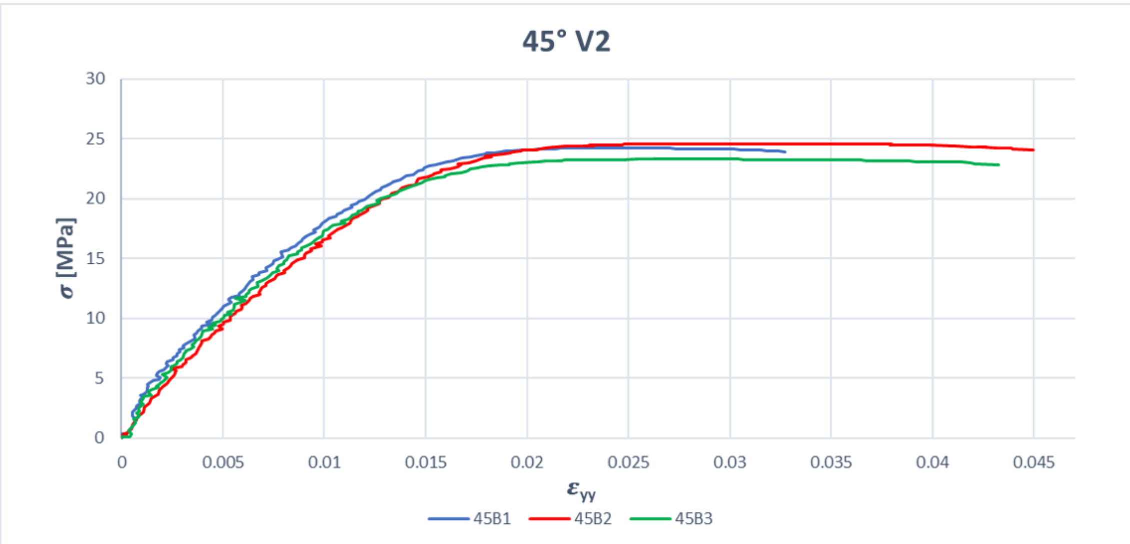

Figure 17: Tensile test of specimens with 45° tilted filament deposition.

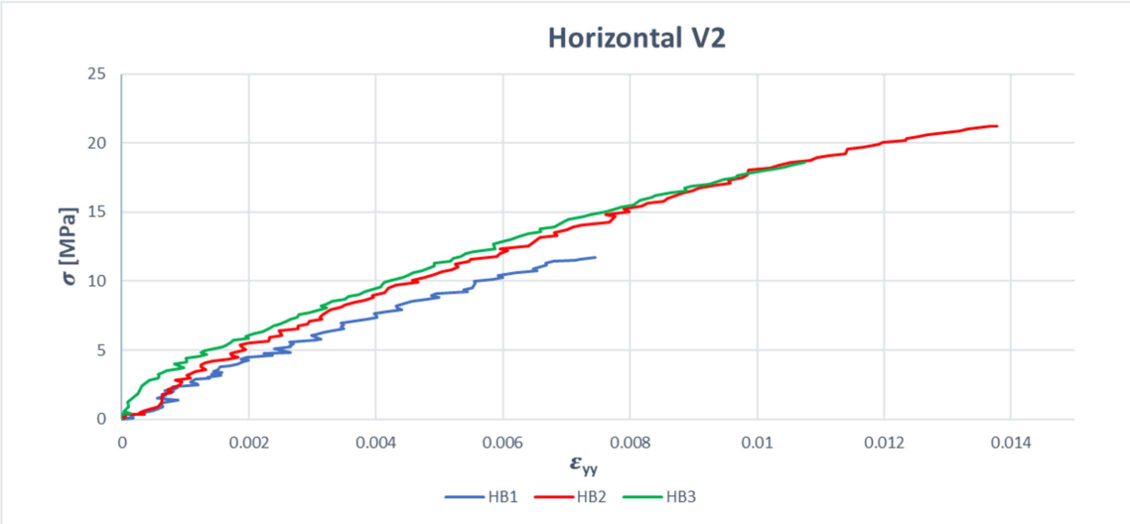

Figure 18: Tensile test of specimens with horizontal filament deposition.

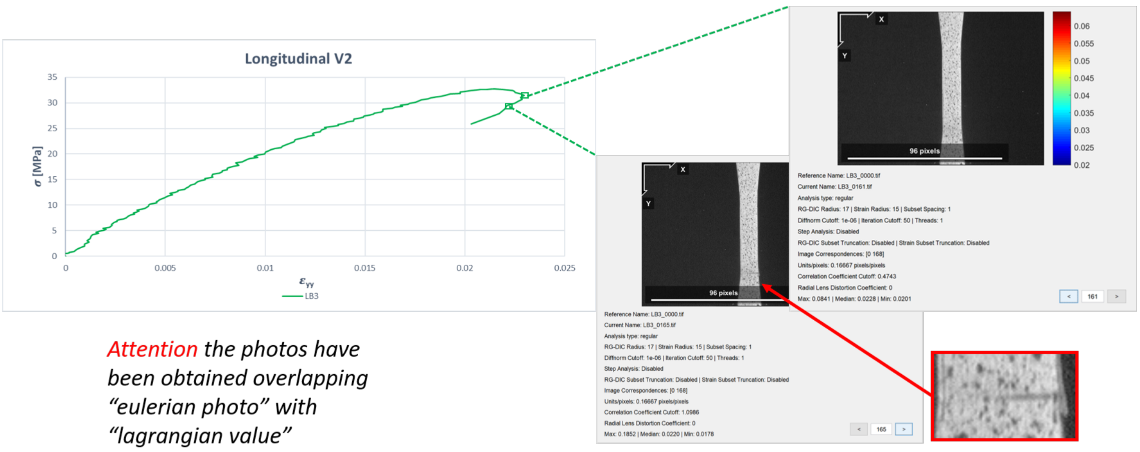

Figure 19: Fracture propagation in tensile specimens.

	Tensile Strength [MPa]		Poisson's Ratio		Elastic Modulus [MPa]	
	Mean Value	Std. Dev	Mean Value	Std. Dev	Mean Value	Std. Dev
Longitudinal	32.4	0.52	0.472	0.011	2541	192
45°	24.0	0.67	0.466	0.059	1181	23
Horizontal	17.2	4.91	0.471	0.049	2546	437

Table 3: Tensile test's outcomes

For what concern the part of the study which is presented in this report the relevant informations yielded by the tensile test were the material parameters. They were in fact necessary in order to compute the fracture toughness of the bending samples. The Young modulus and Poisson ratio of the 45° configuration were thought to be the closest to the bending specimen's case and have then been chosen to implement the furter computations.

Bending Test

For the bending tests a three point bending configuration with pure mode I loading has been adopted, as shown in Fig.20. Three classical specimens, printed conventionally with a ±45° tilted deposition path between two subsequent layers, and three optimized specimens, printed following the innovative technique previously described, were tested. The test has been run with an imposed displacement speed of 0.5 mm/min (as the reference [3]) and 0.5 photos/s were taken with the same camera and the same resolution used for the tensile test. This choice allows to keep the hypothesis of quasi static fracture.

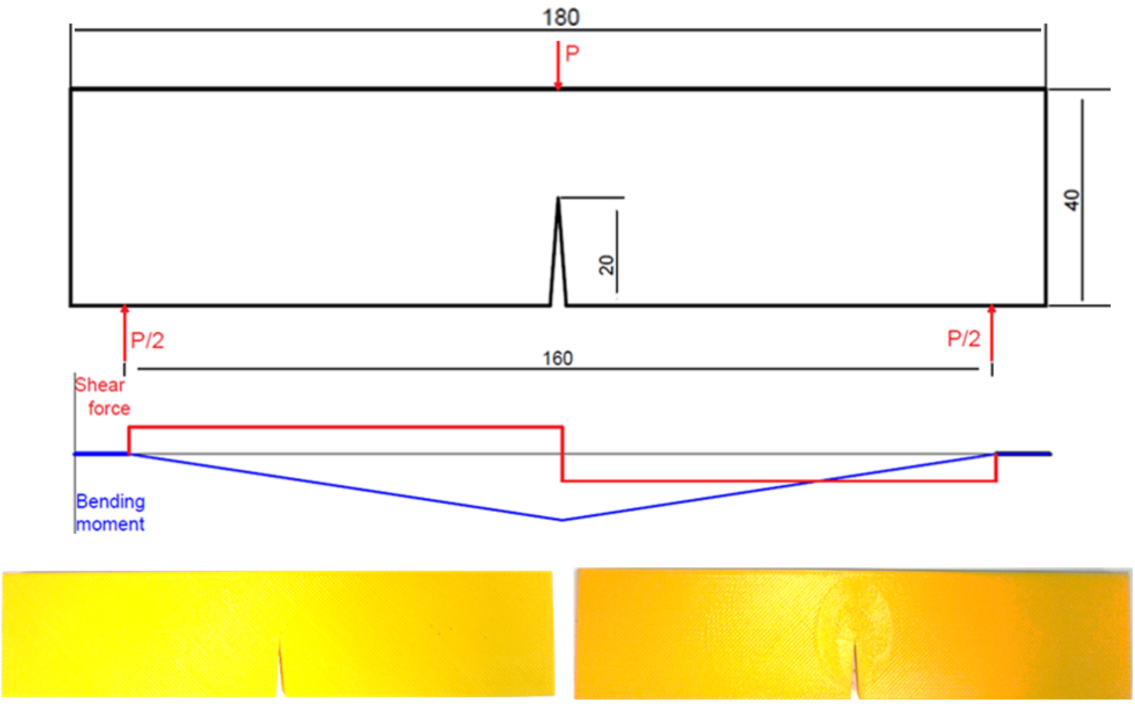

Figure 20: **Top**: Specimen geometry from reference [3] and load case for the bending test. **Bottom**: Classic (left) and optimized (right) specimens.

Analyzing the outcomes of the bending test the first thing that is easy to notice is that all the classical specimens show a similar behavior. Indeed, they all break in the ±45° directions. This might be explained observing that those are the directions of the welding lines. However, this is more likely a shear predominance behaviour, which was unexpected for the present configuration, that is submitted to a purely tensile loading. Anyway the TS (Tension–Shear) transition, or brittle–ductile transition, or mode I/II fracture transition, can occur even though under pure mode I or pure mode II loads

[23]. For a deeper understanding of this change in TS criterion the analysis of the mixity parameter M^p was necessary. Its calculation helps to discern whether the fracture manner will be tensile ($M^p \to 1$) or shear ($M^p \to 0$) and to foresight its direction. Li et al. [23] assessed the bifurcation angle of an elastic–plastic crack in plane strain under mixed mode loading by establishing a criterion in order to study the competition between the tensile fracture (T-type fracture) and the shear fracture (S-type fracture) as function of the mixity parameter M^p. When the crack grows in tensile manner, the maximum circumferential stress criterion is adopted to determine the crack bifurcation angle. When the crack grows in shear manner, the traditional theory of plasticity, according to which the plastic flow develops essentially along one of the slip bands immediately ahead of the crack tip, is used to determine the crack growth direction. It is known that both tensile and shear fracture mechanisms are operative in ductile–brittle regime. The cleavage fracture (T-type fracture) essentially relates to the void growth and coalescence near the crack tip. The ductile fracture (S-type fracture), on the other hand, essentially depends on the plasticity progression. The ductile fracture generally involves a stable crack growth process prior to the occurrence of unstable crack propagation. High fracture resistance is often associated to this kind of fracture, which typically requires an increasing applied load. However, cleavage fracture generally results in rapid loss of load-carrying capacity. Consequently, the onset of cleavage fracture is the critical failure mechanism limiting the load-carrying capacity of the structure. In order to asses fracture resistance in a ductile cracked structure under mixed mode I–II loading, this cleavage-ductile fracture competition must be considered as essential. First, for a given crack under mixed mode I–II loading, we must determine if this is a tensile crack (T-type fracture) or a shear crack (S-type fracture). This is the so called TS (Tension–Shear) transition criterion.

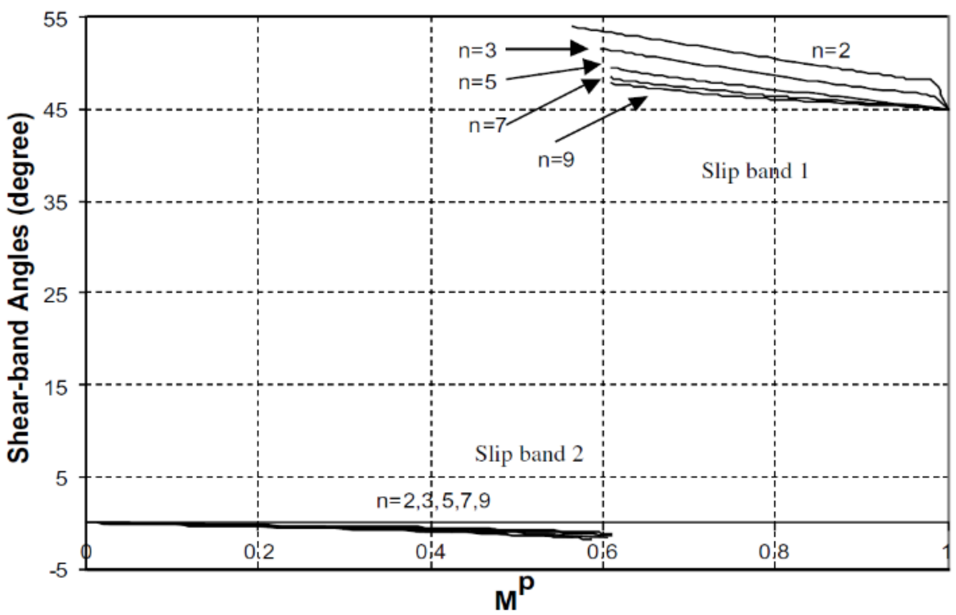

Figure 21: The shear propagation angle in function of the mixity parameter and the hardening exponent n of the material. [23]. In the present experiment the predominant slip band is Slip band 1, due to the high value of M^p that characterizes the bending test configuration.

It is well known that the configuration A is a pure mode I fracture specimen, so it presents a $Mp = 1$ and a propagation angle of 0° with comparison to the vertical direction. However, this does not occur in this case. The most likely explanation is that the τ_c is probably reduced by the welding interface between the filaments resulting in a predominance of the shear manner failure. The slip band criterion says that, in case of shear fracture, the fissure will propagate in the direction of one of the slip bands. For high values of M^p the dominant one (higher stresses) is the Slip band 1, which presents an angle of 45° with respect to the vertical direction (Fig.21).

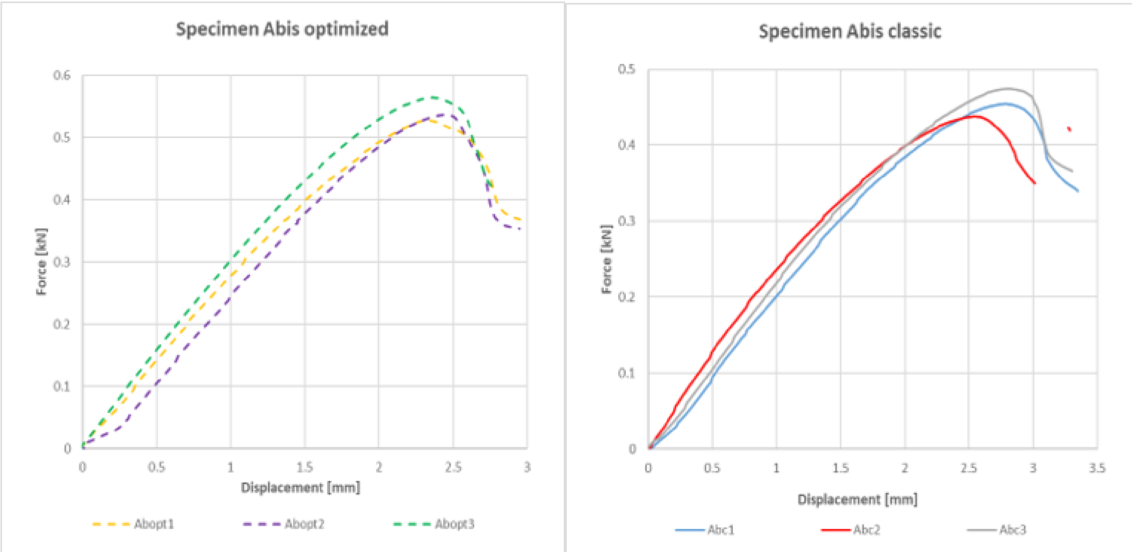

Figure 22: Force-Displacement curve of mode 1 bending specimens. **Left**: The optimized specimens show an higher value of the maximum applied force reached. **Right**: The classical specimens present an higher value of the displacement of the indenter in correspondance of the force peak.

Another quick remark is that thanks to the optimized deposition the fracture starts in correspondance of an higher applied force value but it propagates in a shorter time reaching the peak of the force-displacement curve earlier. This is confirmed by the fact that the fracture is observed at lower machine displacements for the optimized specimens. The results in term of mechanical resistance gain are about ($\sim$ 15%) and an interesting behaviour was highlighted: a failure in shear manner where tensile fracture was expected. Concerning what is happening at the top of the notch it is interesting to see that there is a competition between the fracture starting from the notch and a weakness due to imprecise printing (Fig.23). This internal weakness might explain why, among all the successful optimizations, the optimized specimens presented a lower maximal force's displacement in comparison with the classical geometry.

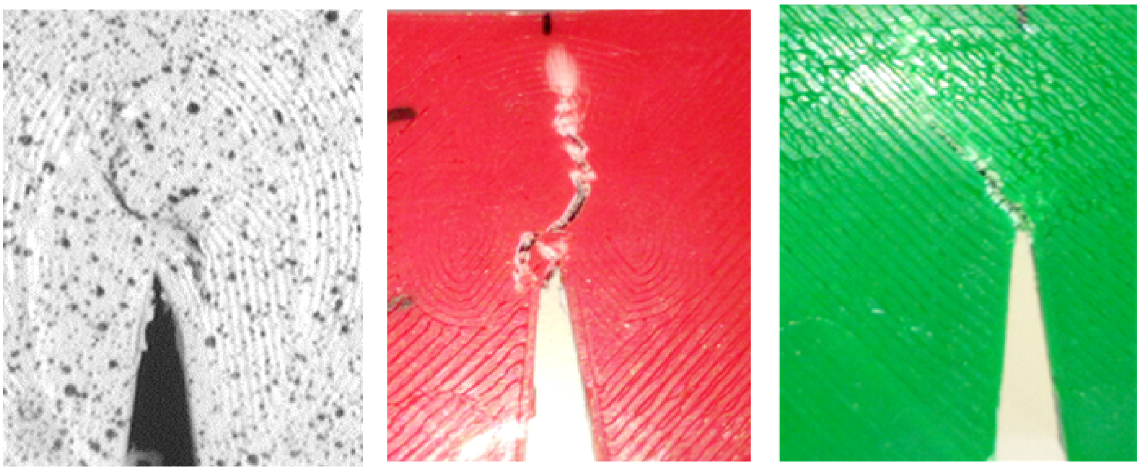

Figure 23: **Left and Center**: In the optimized specimens the fracture start its propagation in correspondance of a weak spot of the welding lines due to printing flaws. **Right**: In the classic specimens the fracture propagates starting from the notch tip.

	Maximal Force	Displ Max
	kN	mm
C1	0.46	2.79
C2	0.44	2.54
C3	0.47	2.82
Opt1	0.53	2.33
Opt2	0.54	2.46
Opt3	0.56	2.35

Table 4: Mechanical test data of all the tested specimens: 3 classical (C) and 3 optimized (Opt).

	Classic	Optimized	Comparison
Built Time	2h 26min	2h 46min	**+13.3%**
Material (mm)	30928	30984	**+0.2%**
Average Mechanical Resistance [kN]	0.46	0.54	**+16.1%**
Average Maximal displacement [mm]	2.72	2.38	**-14.3%**

Table 5: Comparison of conventional and optimized specimens: average printing data and average mechanical test data.

Fracture Toughness Assessment

The majority of the several techniques that have been proposed to extract parameters that quantify the mechanical driving force for fracture can be divided into two main categories [32]:

- The numerical optimization of an assumed SIF value such that the theoretical displacement field matches the measured field.
- The calculation of the energy associated with the changes in the displacement field in order to obtain the strain energy release rate directly. The strain energy release rate may then be converted to a SIF.

The optimization methods require consideration of the fundamentals of linear elastic fracture mechanics, and use techniques that are mathematically quite complex. The application of optimization techniques should be therefore limited to fully elastic fields, and requires accurate location of the crack tip. The application of optimization methods to the calculation of SIF for cracks in quasi-brittle materials may therefore be inaccurate due to difficulties in locating the crack tip.
In contrast to the optimization methods, integral methods can be applied to both elastic and elastic-plastic fields. However, the existing integral methods are mathematically complicated and depend on a presumed stress field around the crack tip.

In this study at first it was decided to adopt an integral method with the aim of computing the change of strain energy density of the specimens undergoing deformation in a manner feasable also in presence of little plasticity conditions. During the work though, the decision shifted toward the doption of an optimization methods due to the impossibility of accurately measure the propagation lenght of the crack. Hence, to reach the final goal of assessing the tested specimens' fracture toughness, multiple trials have been required in order to find a robust method and get reliable results. More than once it has been necessary to change the computation's strategy because of obstacles encountered in the path or because of the inconsistency that the early results presented with respect to previous findings of the research. Another important issue was the precise localization of the actual position of the notch tip whitin the DIC images, which has led to erroneus data. The problem is to be imputed to the low resolution of the DIC images when opened in the graphic user interface of the DIC software and to the natural lack of ideality that commonly characterize physical experiments. In this particular case the misleading reality effect was the presence of paint, required for an effective and meaningful DIC analysis, inside the narrow edge of the notch.

All the main phases of the work have been incorporated in the present chapter in chronological order so to produce a document which covers and summarizes all the activities and intermediate outcomes that have been carried out during the internship. They can be reunited in three different approaches that were attempted and investigated alternatively and in subsequent order: computation of the energy release rate (ERR), analysis of the bending test data, fitting of the measured displacement field. All the cited methods required or an accurate detection of the crack propagation onset or both the latter and a precise measure of the lenght of the propagated crack. In the effort to derive these pivotal informations the DIC images have been carefully examinated. Unfortunately it is not been possible to detect exactly the particular DIC image corresponding to the crack onset, but rather a sufficiently small range of images was selected in order to compute a statistical value of the fracture toughness for each specimen. The difficulty is given by the extreme resemblance between subsequent snapshots, due to an high frequency of shooting, and by the fact that sometimes, especially for the optimized specimens, the crack doesn't start its propagation from the notch tip, but in correspondance of a printing flaw (like an air gap) that provokes a marked weakness in the welding lines. It is also possible that the crack would open almost simultaneously in multiple spots.

In the first phase we tempted to compute the J-integral by mean of the calculation of the ERR, with whom it is strictly related and which requires exclusively the DIC data. In a second phase we tried to compute the J-integral using a well known formula that requires mechanical test data, as applied force and indenter displacement, and DIC data. In the last, and more successfull, attempt we employed a numeric method which requires only DIC data to compute the SIF. The first two methods were strongly and negatively influenced by the aforemensioned paint problem, but, the real reason why they were abandoned is placed in the present impossibility of measuring the crack lenght with sufficient accuracy.

All the listed analysis share the same initial steps. For writing convenience they will be addressed now at once.

Initial Steps of the Study

To implement the various computations that will lead to the desired outcomes and to develop further considerations, it is foremost necessary to set, one specimen at a time, a consistent DIC analysis. Therefore, the resulting DIC data are made accessible within the matlab environment through the call of specific commands.

DIC Analysis

Parameter	Value
RG-DIC radius	*17*
Strain radius	*15*
Subset spacing:	*2*
Step analysis	*Disabled*
Radial Lens Distortion Coefficient	*0*
Subset Truncation	*Enabled*
Correlation Coefficient Cut-off	*0.5*

Table 6: DIC analysis parameters.

The DIC analysis was carried out using the software Ncorr, which present a pretty intuitive graphic user interface (GUI). The snapshots taken during the test of a certain specimen were first uploaded in the software: the first snapshot was chosen as reference frame, a set of immediately following snapshots as current images. The first $200 - 250$ snapshots have always been uploaded as current images for each analysis, spanning from the undeformed configuration of the specimen to a snapshot taken in correspondance of an instant successive to the peak in the force-displacement curve. In this way the whole part of the experiment interesting for the evaluation of the fracture toughness was taken into account by the analysis, while the snapshots related to the descending part of the force-displacement curve, when the beam is already cracked and the peak force has already been reached, were neglected to reduce significantly the processing time.

When the upload is completed it's necessary to draw the desired region of interest (ROI), which identifies the part of the image that will be processed by the DIC software. In this phase it must be taken in consideration the entity of the area that we are interested to. The not patterned parts have to be excluded and, in relation to the kind of data that we want to extract and the type of fracture behavior, the convenience of including in the ROI the plasticity area has to be evaluated. In fact in case of plastic deformation the model and physic relations that Ncorr uses to extract the strain field are no more valid.
After usefully setting the DIC parameters (subset radius, subset spacing, strain radius,

correlation coefficient cut-off) and after completing the analysis, it is possible to plot the displacement and strain fields directly in the Ncorr interface. This is useful to have a first check of the process quality and of the presence noisy data. The computable fields are: u and v displacement, exx, eyy and exy strain. Informations about the specimen's third dimension are not provided by this technology but, within the assumption of plane stress condition, they are irrelevant.

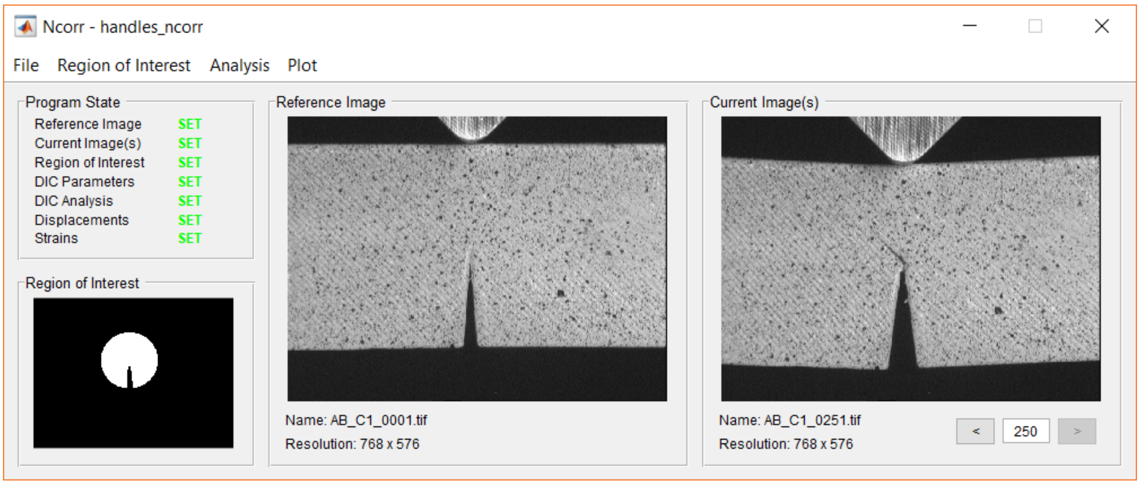

Figure 24: Ncorr graphic user interface. **Left**: undeformed specimen as reference image **Right**: 250 current images uploaded (the last one uploaded is shown in the GUI).

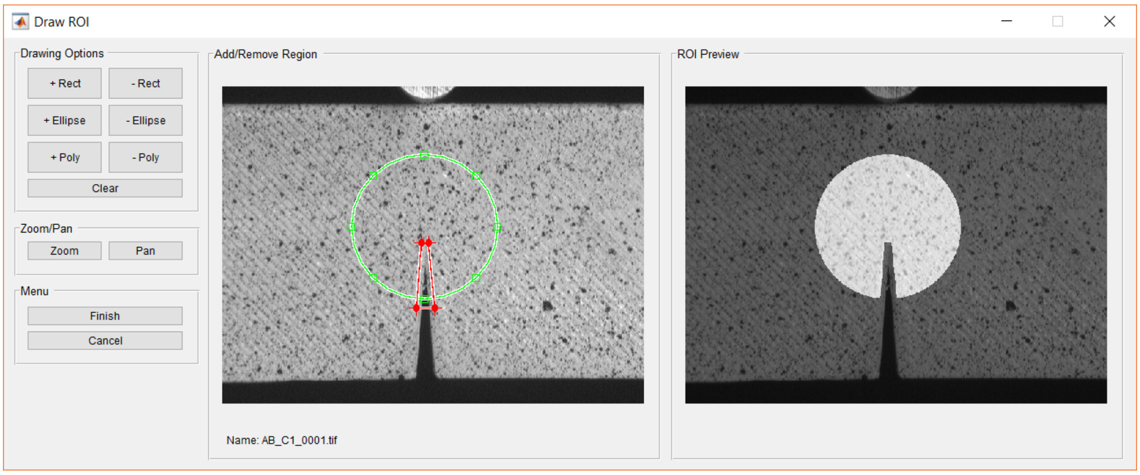

Figure 25: Ncorr: drawing the region of interest (ROI).

For this experiment it was chosen to use a single camera, and not a stereoscopic configuration, in order to acquire and analyse the data faster and to obtain better quality images. Beside, since the specimens are quite thin its behaviour can be approximated to plain stress. The additional information offered by a stereoscopic configuration would be of no use, as what is happening in the thickness does not deeply interest us.
Since the entity of the strains for ABS specimens are important but still lower compared to other polymers, a pattern composed of thin dots was required.

Finally, to set the measurement, it is necessary to take a reference photo where it is also possible to define a scale between millimeters (real distance units) and pixels (photo units). This has been done by taking a picture of a ruler beside the specimen and manually counting the correspondence between the two units of measure. Once the scale value has been stated the value measured in millimiters will be directly yielded and plotted by the software.

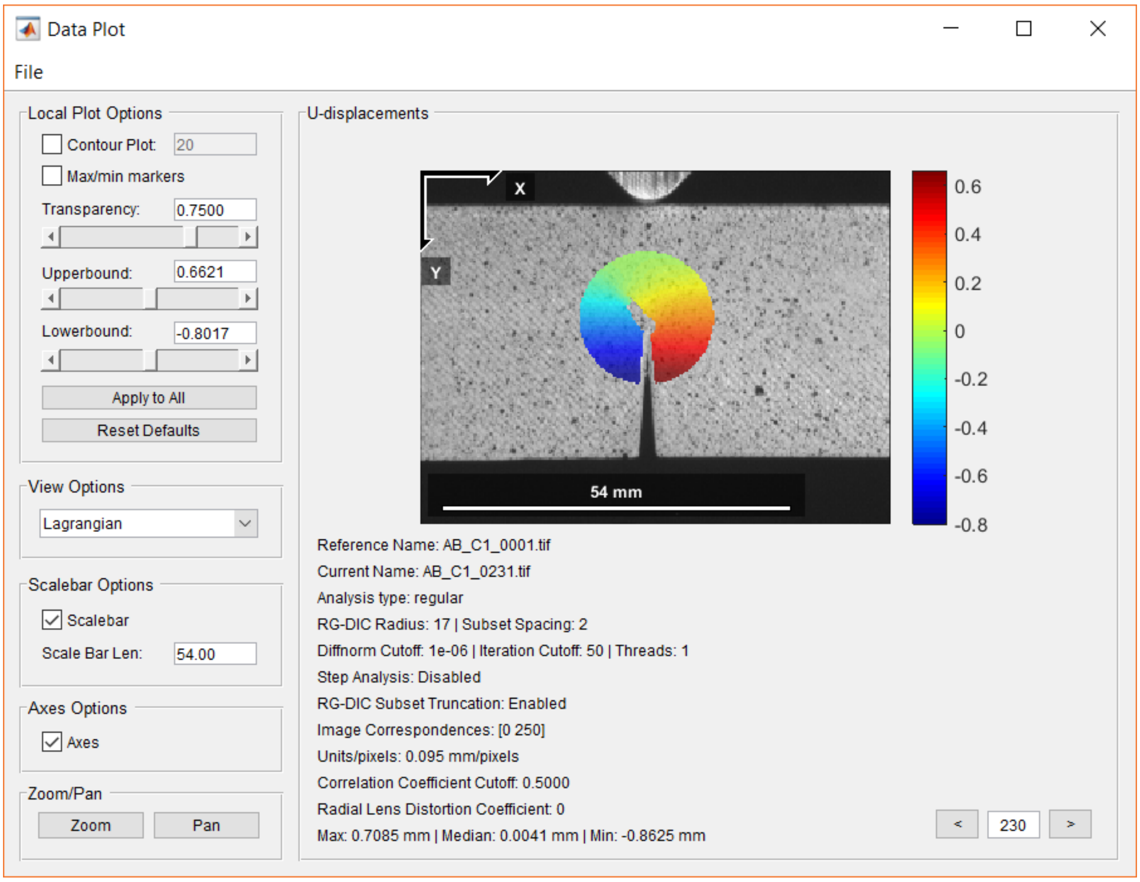

Figure 26: Ncorr: V displacement plot (here is labeled as U-displacement because the reference frame of Ncorr is tilted with respect to the reference frame that we set on the notch tip).

DIC Data Extraction

With some quick commands the DIC data are finally available and usable in the matlab environment. The initial steps of the DIC analysis that were common for the three different computational approaches end with the writing of this preliminary code and going forward from here the processes distinguish one from the other. With this script is possible to state the material parameters, that were previously measured with the tensile test, to select from the DIC input data only the active subsets (those included in the ROI) and to set the reference frame in the desired position (the one corresponding to the conventional reference frame of fracture mechanics).

In the following pages the three investigated methods will be widely described, but not before having clarified the issue that negatively influenced the results of the first two of them: the wrong position of the notch tip.

```
clearvars -except handles_ncorr

% material properties (homogeneus, isotropic model)
E = 2.541*10^9;  % Young modulus [Pa]
ni = 0.472;          % Poisson ratio
mi = E/(2*(1+ni));  % Shear modulus [Pa]

% load from Ncorr displacement and strain data of a certain DIC image
scale = handles_ncorr.data_dic.dispinfo.pixtounits*0.001; % measured by mean of Inkscape [m]
spacing = handles_ncorr.data_dic.dispinfo.spacing; % subset spacing
image = 37; % number of the selected current image
disp_x = handles_ncorr.data_dic.displacements(image).plot_u_ref_formatted*0.001; % [m]
disp_y = handles_ncorr.data_dic.displacements(image).plot_v_ref_formatted*0.001; % [m]
strain_xx = handles_ncorr.data_dic.strains(image).plot_exx_ref_formatted;
strain_xy = handles_ncorr.data_dic.strains(image).plot_exy_ref_formatted;
strain_yy = handles_ncorr.data_dic.strains(image).plot_eyy_ref_formatted;
[m,n] = size(strain_xx); % matrix representing the entire DIC image

k = 1;
for i=1:1:m % row-major indexing
    for j=1:1:n
        if(strain_xx(i,j)~=0)  % condition to exclude the subsets outside the ROI
            Y(k) = (i-1)*(spacing*scale); % kth subset cartesian coordinate [m]
            X(k) = (j-1)*(spacing*scale);
            U(k) = disp_x(i,j); % kth subset displacement component [m]
            V(k) = disp_y(i,j);
            exx(k) = strain_xx(i,j); % kth subset strain component
            exy(k) = strain_xy(i,j);
            eyy(k) = strain_yy(i,j);
            ezz(k) = -ni/(1-ni)*(exx(k) + eyy(k));
            k = k+1;
        end
    end
end

% the notch tip coordinates are manually detected in the Ncorr's plot
tip_x = (124-1)*spacing*scale;
tip_y = (103-1)*spacing*scale;
% new reference frame set in the notch tip
Yc = Y - tip_y;
Xc = X - tip_x;
% polar coordinates
R = sqrt(Xc.^2+Yc.^2);
theta = atan2(Yc,Xc) + pi/2.0; % with respect to the notch tip plane
```

Figure 27: Matlab code for DIC data extraction and preliminary manipulations.

Misleading Notch Tip Positioning

As previously explained, the DIC analysis operates analyzing the grey scale of the pattern painted on the surface of the sample. This of the painting is a fundamental step of the process because allows to have a reliable evaluation of the deformation of the sample during the mechanical test. Unfortunately the notched shape of the specimens in exam is very incline to create problems with this procedure because of the extreme difficulty in removing the paint from the narrow edge of the notch. Although the efforts, it was impossible to completely remove the paint from that thin aperture. Therefore the notch tip position, as far as can be approximately guessed with the naked eye, wasn't easy to detect due to the DIC image resolution. That led to a distorted localization of the notch tip for all the specimens: for instance it led to consider the notch as $2-3$ mm shorter than it really was for all the specimens. Figure 28 shows the preliminary step of DIC analysis: the insertion of a ruler in the undeformed image in order to measure the image scale, necessary to identify the conversion between pixels and millimeters. Hence, with a basic tool of computer graphic it's easy to measure the scale ratio.

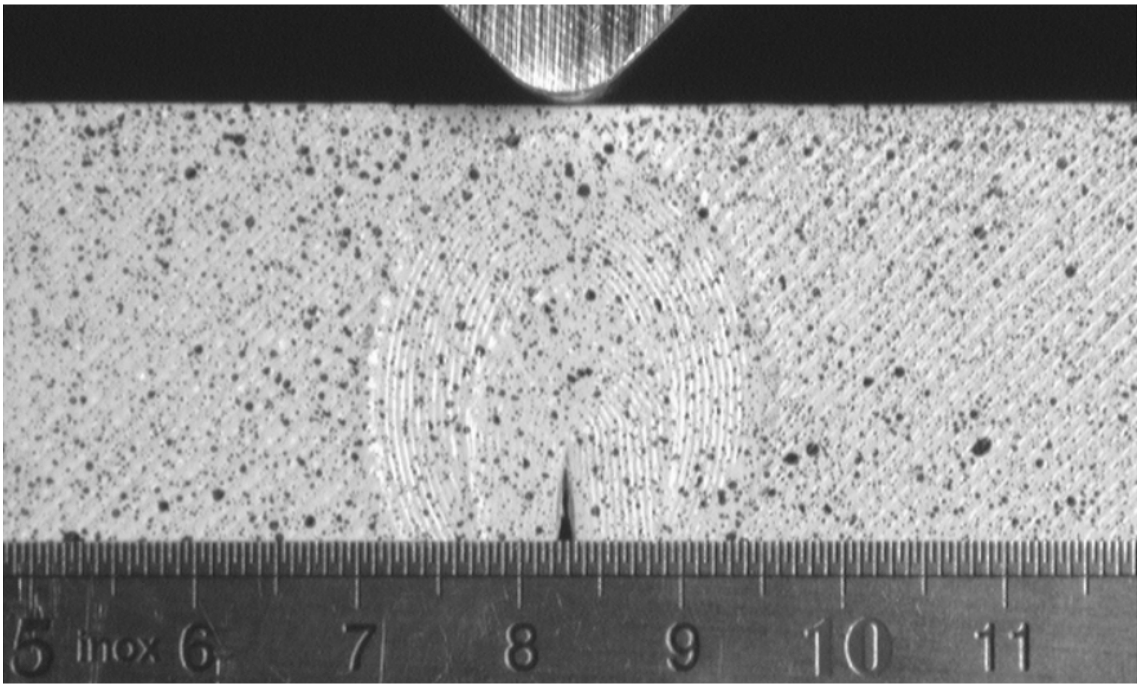

Figure 28: Ruler inserted in the undeformed specimen's image in order to define the scale.

Figures 29 and 30 represent instead the detection of the systematic error that was made at the beginning of the study and the subsequent editing of the ROI. The problem was solved simply by checking the printing quality and manually verifying the respect of the theoretical dimensional specifics of the specimens, measuring them on the unpainted side. It has been confirmed that the notches present the expected lenght, with a tolerance grade of 0.5 mm. As it is possible to see in the left part of fig. 30, the resolution of the image opened in the graphic interface of Ncorr does not allow to localyze precisely the notch tip and, so, only by an eye checking of the part it was possible to clear the doubts. Hence, from this moment forward the notch tip position within the Ncorr image was not anymore selected by eye, but it was chosen in correspondance of the theoretical position it should occupy: at half of the width of the specimen. The ROI has then been modified as shown in fig. 30 and a new DIC analysis has been carried out.

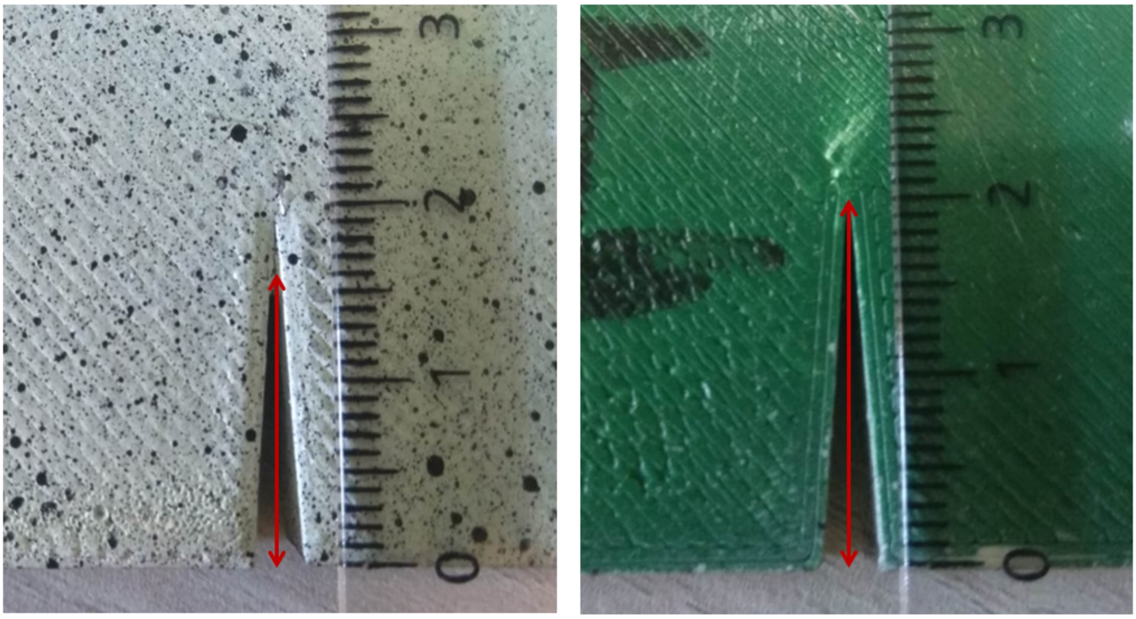

Figure 29: The notch looks a few millimiters shorter due to the presence of paint in the slot. **Left**: Painted side of the specimen. **Right**: Clean side of the specimen.

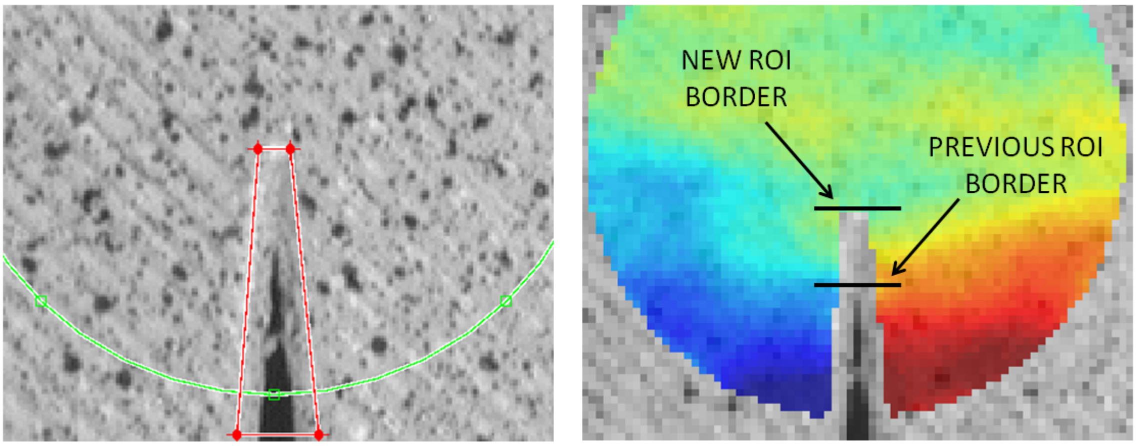

Figure 30: **Left**: Drawing a new ROI in Ncorr. **Right**: Different localization of the wrong and correct notch tip.

The problem that this misdetection has generated in the continuation of the study is due to the fact that, for both the energy release rate (ERR) computation and the J-integral formula based on the mechanical test data, the crack lenght is necessary. Having considered the notch tip to be in a position lower with respect to the actual one, we measured in the DIC image a crack lenght that was always overestimated and, as a consequence, we considered the crack to open much earlier than the reality, resulting in fracture toughness values significantly underextimated. In fact, because of this mistake, we were not measuring the specimen's crack growth, but the cracking of the paint that precedes the crack onset added to the actual crack growth. In all cases we were led to state that the specimens start to crack before the 100th snapshot, which afterwards was demonstrated to never be the case.

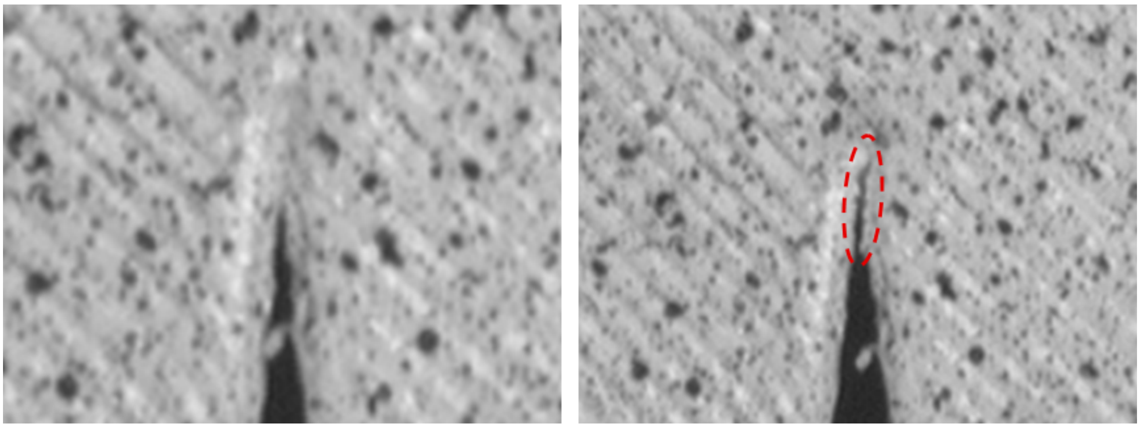

Figure 31: Paint cracking: at the moment of this snapshot the specimen is still uncracked and the circled crack should be subtracted from the final measure of the specimen's crack.

Thus the ERR and J-integral results gathered with the first two methods adopted, which are clearly affected from this prior misunderstanding, should not to be taken in much consideration. In addition to this mistake, the actual factor that couldn't allow to estimate a reliable value of fracture toughness following one of these two approaches was the impossibility of an accurate measurement of the crack lenght. The latter is the real reason that led to abandon these two computational methods. The processes used to compute them are instead worthy of review because they could result in a valid support in a future study in which the precise crack lenght measure issue would be overcome.

First Approach: Energy Release Rate

The strain energy release rate,or simply energy release rate (ERR), is the energy dissipated during fracture per unit of newly created fracture surface area. This quantity is central to fracture mechanics because the energy that must be supplied to a crack tip for it to grow must be balanced by the amount of energy dissipated due to the formation of new surfaces and other dissipative processes such as plasticity. The energy release rate is directly related to the stress intensity factor associated with a given two-dimensional loading mode (Mode-I, Mode-II, or Mode-III) when the crack grows straight ahead. This is applicable to cracks under both plane stress and plane strain conditions. For Mode-I, under plane stress conditions, the energy release rate G is related to the Mode-I stress intensity factor K_I for a linearly-elastic material by

$$G = \frac{K_I^2}{E} \tag{17}$$

There are a variety of methods available for calculating the energy release rate given material properties, specimen geometry, and loading conditions. Some are dependent on certain criteria being satisfied, such as the material being entirely elastic or even linearly-elastic, and/or that the crack must grow straight ahead. A method that works arbitrarily is that calculating the total potential energy and differentiate it with respect to the crack surface area. This is typically done by calculating the stress field resulting from the loading and then calculating the strain energy in the material resulting from the stress field. Using DIC we dispose of the strain fields, instead of the stress fields, and using the Hook's law (in case of linearly elastic material) it is possible to express the strain energy density as function of the strain fields.

The strain-energy density of a material is defined as the strain energy per unit volume and it is equal to the area under the stress-strain curve of a material. Thus, if SI metric units are used, the strain-energy density is expressed in J/m^3. If we apply a load to a material it will deform. The units of energy are force·distance, so when a load is applied and the material deforms, we are putting energy into the material. This energy introduced into the material due to the loading is referred to as “strain energy.” We prefer to normalize strain energy by unit volume, and when we do so, this is referred to as strain energy density.

The difference is given by the strain energy density before the propagation subtracted by the strain energy density after the propagation because the mechanical test is displacement controlled (potential energy Π= strain energy density U).

$$G = -\frac{d\Pi}{dA} = -\frac{d\Pi_b - d\Pi_a}{dA} = \frac{d\Pi_a - d\Pi_b}{dA} \tag{18}$$

The ERR is an energy over area as unit of measure. The computational strategy adopted in the matlab script consisted in computing the strain energy density in each subset (energy over volume), sum the values of all the subsets of the ROI, multiply by the area of each subset (energy over lenght) and finally divide the result by the measured crack lenght (energy over area).
The first thing to do was to detect the onset of the crack's propagation. In fact, in order to implement the ERR approach the total lenght of the crack between two points was required. The strategy to obtain the ERR for the specific specimen consisted of two main steps: to compute the total strain energy density contained in the given ROI (the one used in the DIC analysis) in correspondance of two successive instants, to multiply them by the area of the ROI and to divide the difference between the two values by the new formed crack area. The two aforemensioned instants are the onset of the crack's propagation and an instant after that the propagation has increased the crack lenght of a certain value. To get results as accurate as possible the lenght of propagation taken into account should not be too long because only informations related to the start of propagation are needed (in an ideal case we would not want to use lenghts longer than a millimiter). Moreover it's necessary that the lenght in exam would be as straight as possible as in case of pure tensile mode fracture. This process presented more than one obstacle to be completed and at the end, because of these issues, another approach was preferred. One problem was related to the identification of the exact position of the notch tip, which was necessary to measure correctly the crack lenght. In this very step the problem related to the paint was very influential because led to completely overextimate the crack lenght (of about 2 mm on average). Another problem was that it was very offen impossible to detect a lenght shorter than 1 mm because the material used to open in small segments and not gradually. Furthermore, the crack path was not perfectly straight but it was quite irregular in the small scale so that the measurement of the exact lenght resulted impossible. Anyway, without the misdetection of the notch tip position it is fair to think tht we could have gotten approximated results of decent quality.
Two different kinds of ROI were used in the attempt of computing the ERR: one circular (including the plasticity area) and one annular (excluding the plasticity area). The inner and outer radii have been chosen randomly though (anyway the inner radius of the annular ROI is much bigger than the area we would like to avoid).

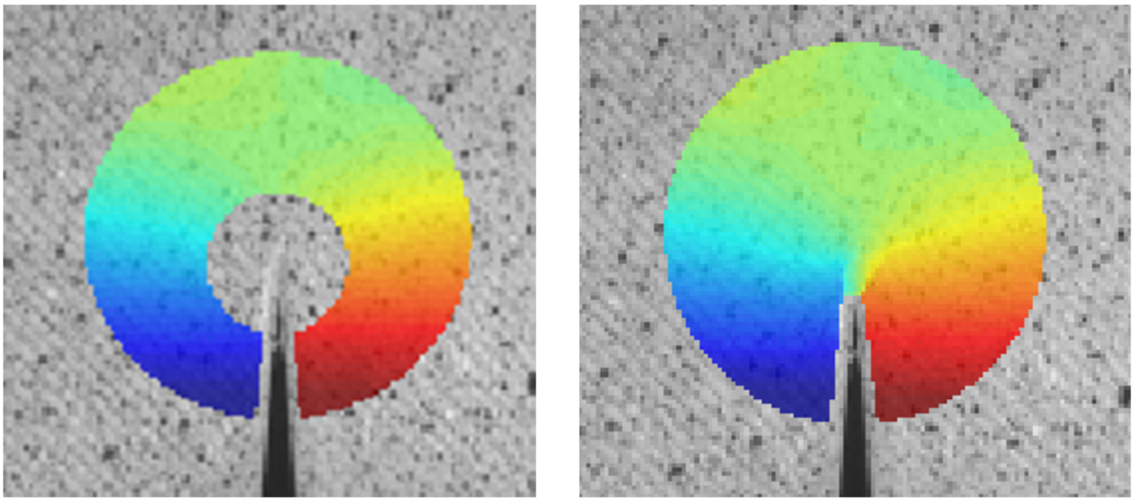

Figure 32: The two different regions of interest used in the DIC analysis to collect data for the computation of the energy release rate.

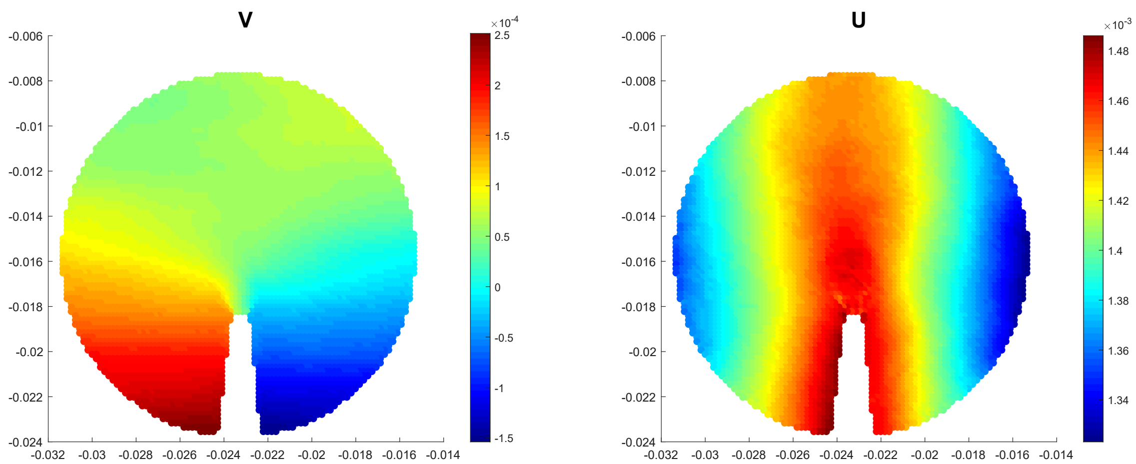

Figure 33: Displacement fields inside the ROI. The coordinates are negatives and not centered because in this phase the reference frame was still the one of Ncorr.

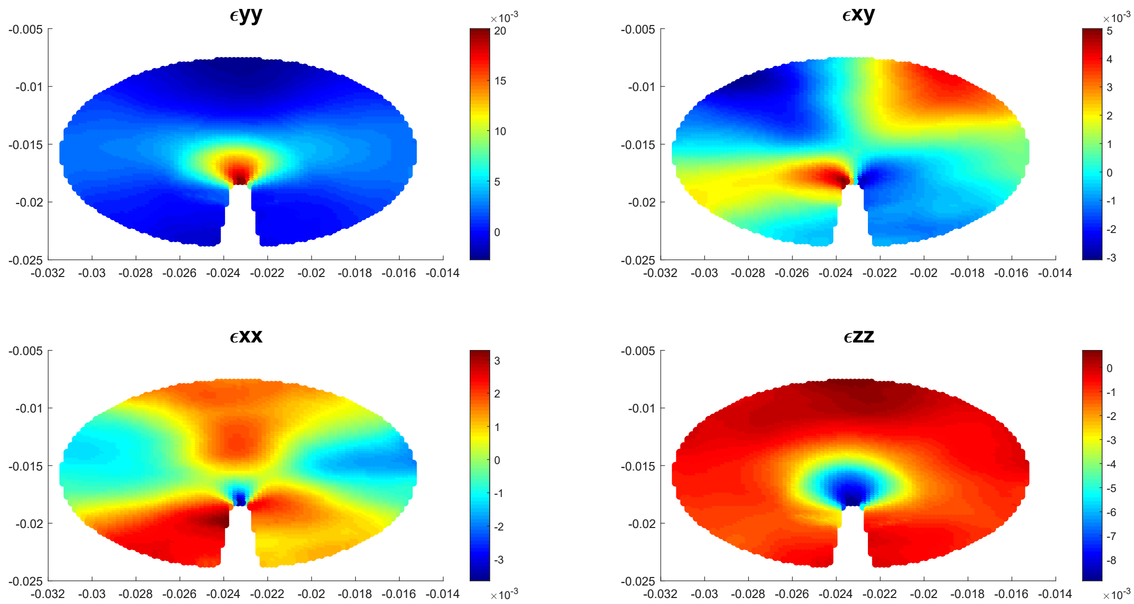

Figure 34: Strain fields inside the ROI (ϵ_{zz} is been computed because Ncorr doesn't yield it. The coordinates are negatives and not centered because in this phase the reference frame was still the one of Ncorr.

```
L = 0.0012; % [m] (measured by eye with Inkscape)
u1 = zeros(1,N);
u2 = u1;
s = (spacing*scale)^2; % area of a single subset [m^2]

% STRAIN ENERGY DENSITY [J/m^3]

for k=1:1:N % 3D model

    % Using the strain fields of the DIC image corresponding to the crack onset
    u1(k) = ni*mi/(1-2*ni)*(exx1(k)+eyy1(k)+ezz1(k))^2+mi*(exx1(k)^2+eyy1(k)^2+ezz1(k)^2)+2*mi*exy1(k)^2;

    % Using the strain fields of the DIC image corresponding to the end of a straight propagation path
    u2(k) = ni*mi/(1-2*ni)*(exx2(k)+eyy2(k)+ezz2(k))^2+mi*(exx2(k)^2+eyy2(k)^2+ezz2(k)^2)+2*mi*exy2(k)^2;
end

for k=1:1:N % 2D model (ezz is neglected)

    % Using the strain fields of the DIC image corresponding to the crack onset
    u1(k) = ni*mi/(1-2*ni)*(exx1(k) + eyy1(k))^2 + mi*(exx1(k)^2 + eyy1(k)^2) + 2*mi*exy1(k)^2;

    % Using the strain fields of the DIC image corresponding to the end of a straight propagation path
    u2(k) = ni*mi/(1-2*ni)*(exx2(k) + eyy2(k))^2 + mi*(exx2(k)^2 + eyy2(k)^2) + 2*mi*exy2(k)^2;
end

% ENERGY RELEASE RATE [J/m^2]
ERR = s*(sum(u1)-sum(u2))/L; % s brought outside because the area of each subset is the same
```

Figure 35: Matlab code used to compute the strain energy density before and after the crack's propagation, needed to obtain the energy release rate.

Second Approach: Mechanical Test Data

Once the energy approach was abandoned, the output data of the bending test were exploited to evaluate the fracture toughness of the specimens. In this case the DIC analysis was not strictly necessary since the only datum that was missing in the mechanical test data was the crack lenght, which could be measured without the help of DIC. However, DIC was used again in this occasion in order to measure the displacement of the indenter of the bending machine: this passage was necessary to check if the machine had registered precise values of the indenter's displacement.

The information gathered during the test are the force applied and the indenter's displacement registered by the bending machine. Hence the force-displacement curves are obtained for each specimen.

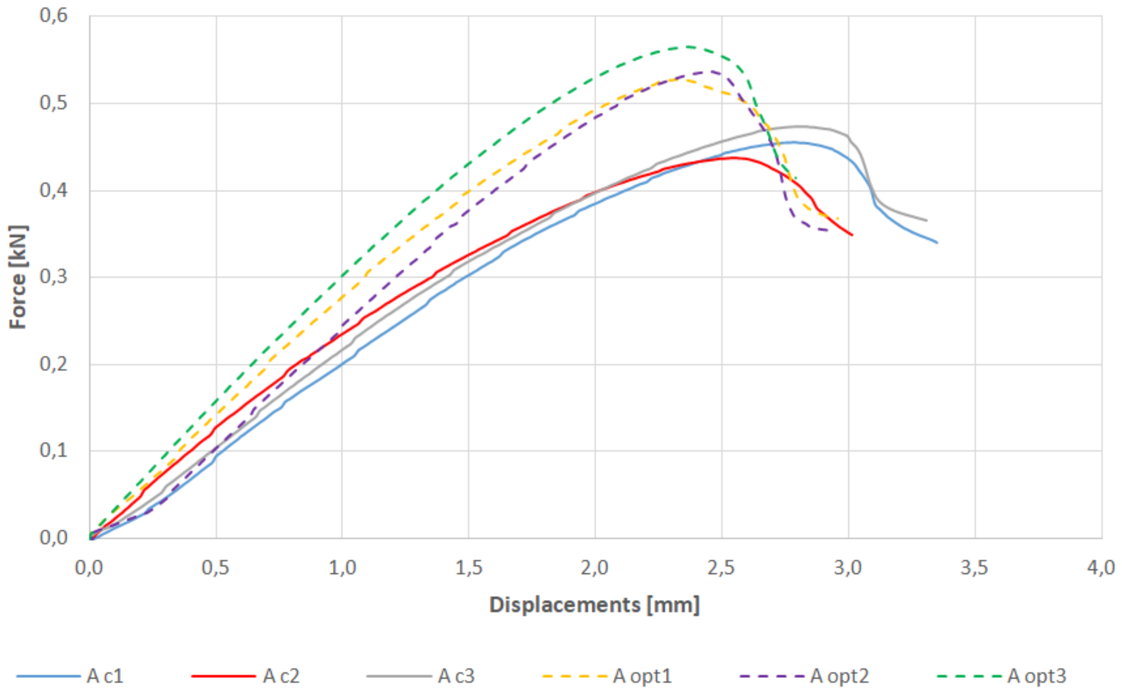

Figure 36: Applied force registered by the bending machine versus displacement of the machine's indenter. In the mechanical test the displacement rate was imposed: the registered force depends by the resistance offered by the specimen.

Standard Test Method

The formula used to compute the SIF and J integral was taken from ASTM International [35] because the geometrical specifications of the specimens and of the bending test match the ones prescribed by the standard test method.
The standard bend specimen is a single edge notched and fatigue-cracked beam loaded in three-point bending with a support span, S, equal to four times the width, W. The general proportions of the specimen configuration are shown in Fig.37. Alternative specimens may have $1 < W/B < 4$. These specimens shall also have a nominal support span equal to $4W$.

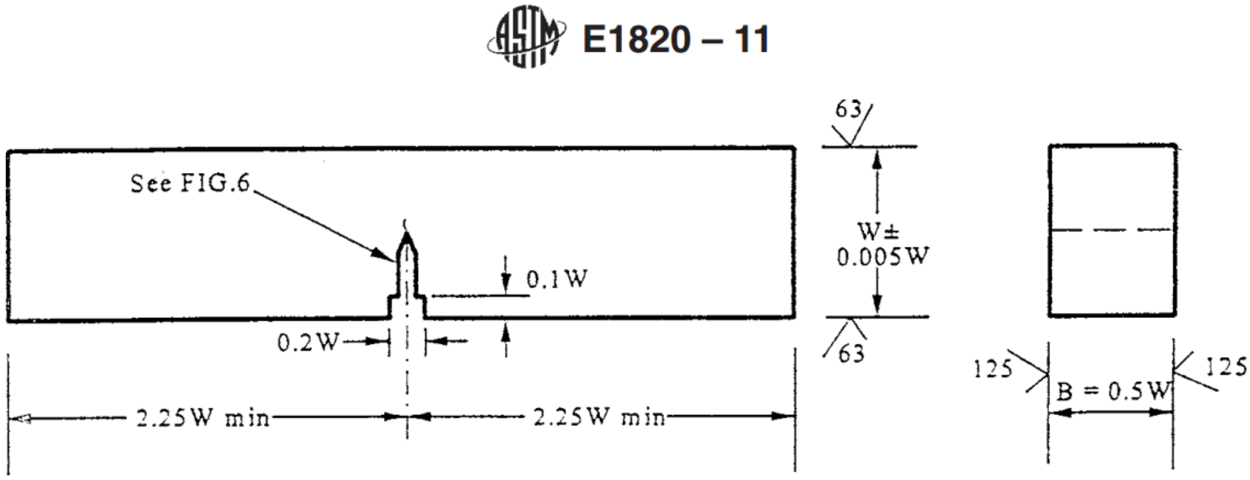

Figure 37: Recommended Single Edge Bend Specimen [35].

Calculation of K For the bend specimen at a force $P_{(i)}$, calculate K as follows:

$$K_{(i)} = [\frac{P_i S}{(BB_N)^{1/2} W^{3/2}}] f(a_i/W) \tag{19}$$

where:

$$f(a_i/W) = \frac{3(\frac{a_i}{W})^{1/2}[1.99 - (\frac{a_i}{W})(1 - \frac{a_i}{W})(2.15 - 3.93(\frac{a_i}{W}) + 2.7(\frac{a_i}{W})^2)]}{2(1 + 2\frac{a_i}{W})(1 - \frac{a_i}{W})^{3/2}} \tag{20}$$

J Calculations for the Basic Test Method: For the single edge bend specimen, calculate J as follows:

$$J = J_{el} + J_{pl} \tag{21}$$

where:

- J_{el} = elastic component of J

- J_{pl} = plastic component of J

At a point corresponding to v and P on the specimen force versus displacement record, calculate the J integral as follows:

$$J = \frac{K^2(1-\nu^2)}{E} + J_{pl} \tag{22}$$

$$J_{pl} = \frac{\eta_{pl} A_{pl}}{B_n b_0} \tag{23}$$

where:

- A_{pl} = area under force versus displacement record as shown in Fig.38

- η_{pl} = 1.9 if the load-line displacement is used for A_{pl}

- B_N = net specimen thickness ($B_N = B$ if no side grooves are present)

- $b_0 = W - a_0$.

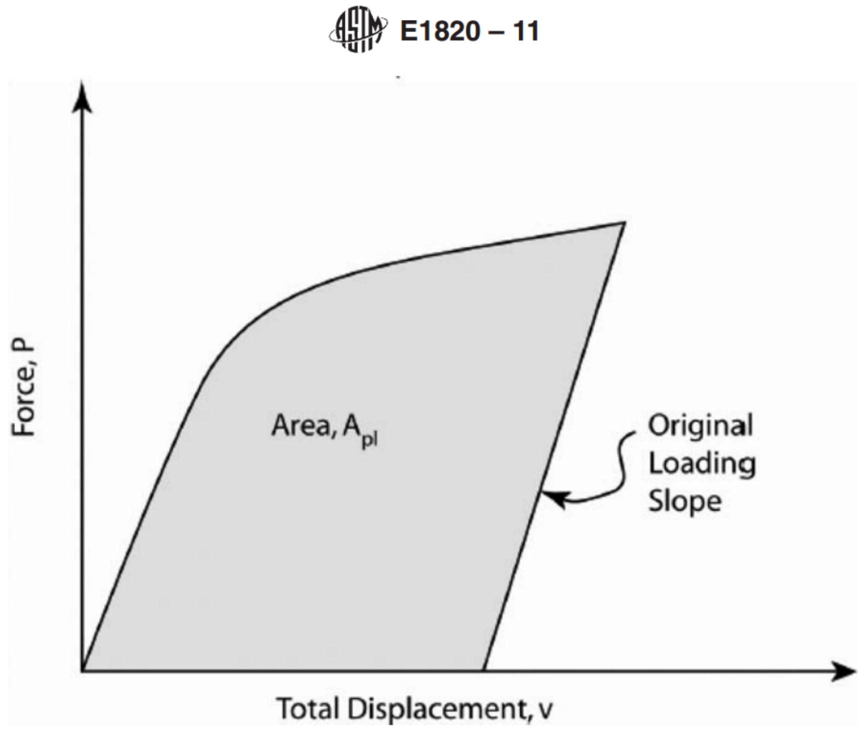

Figure 38: Definition of area A_{pl} for J Calculation Using the Basic Method of [35].

Critical Stress Intensity factor and J Integral

In the computation of K using eq. 19 it was necessary to know the crack lenght in that particular moment. It was obtained with the time laws of the indenter's displacement and of the frequency of DIC image capture. As already stated in the previous works's section, the test has been run with an imposed displacement speed of 0.5 mm/min and 0.5 photos/s were taken. To compute K_I as close as possible to the crack onset, so to evaluate its critical value K_{Ic}, the shortest crack propagation detectable by eye was chosen to start te procedure. From the latter the number of the related image was found and consequently the displacement value (fig. 39). The displacement value is coupled with a force value registered in the same instant by the machine and so all the parameters needed in the formula are now available.

K computed close to the start of crack propagation							
	[mm]		n°	[s]	[mm]	[kN]	[Mpa*m$^{1/2}$]
	a	a/W	Shot	Time	disp matlab	F *	K
c1	20,46	0,5115	70	140,0	1,017	0,2047	1,1197
c2	21,40	0,5350	70	140,0	1,069	0,2477	1,4640
c3	21,61	0,5403	70	140,0	1,053	0,2313	1,3917
opt1	21,18	0,5295	122	244,0	2,036	0,4980	2,8900
opt2	21,39	0,5348	118	236,0	1,790	0,4448	2,6274
opt3	21,82	0,5455	100	200,0	1,597	0,4512	2,7640
c_AV	21,16	0,5289			1,0461	0,2279	1,3251
opt_AV	21,46	0,5366			1,8077	0,4647	2,7605
RATIO	1,01	1,0145			1,7280	2,0391	2,0832

Script matlab

Figure 39: Procedure to compute the critical value of SIF. From a given crack lenght the image number was found and through the matlab script in fig. 42 the displacement of the indenter was obtained.

J computed at Fmax							
		[kN]	[mm]	[mm*kN = J]	[mm*kN = J]	[J]	[kJ/m^2]
	linear slope (m)	F	disp	isosceles area	total area	A_{pl}	J
c1	0,0934	0,3855	2,79	0,0481	0,7318	0,6837	6,8146
c2	0,0722	0,3997	2,54	0,1186	0,6814	0,5628	5,9494
c3	0,0981	0,3980	2,81	0,0585	0,7862	0,7277	7,4374
opt1	0,1095	0,4929	2,32	0,0969	0,7077	0,6109	8,3006
opt2	0,1097	0,4856	2,46	0,0523	0,7224	0,6701	8,4144
opt3	0,0961	0,5321	2,36	0,1359	0,7852	0,6493	8,4441
c_AV	0,0879	0,3944	2,713		0,7331	0,6581	6,7338
opt_AV	0,1051	0,5035	2,380		0,7384	0,6434	8,3864
RATIO	1,1957	1,2767	0,877		1,0072	0,9777	1,2454

Figure 40: The J integral was computed at maximum applied force. Area A_{pl} was measured by subtracting the isosceles area subtended to the linear part of the curve from the total subtended area (fig. 38).

The indenter's displacement was computed with matlab supposing that it was equal to the maximum displacement value present among all the active subsets of the given DIC image.

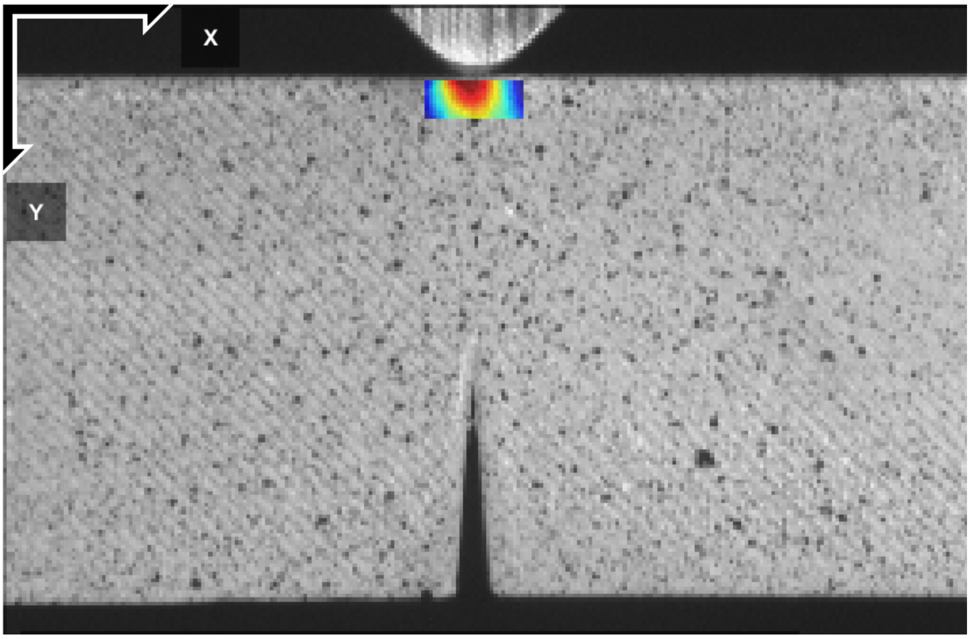

Figure 41: Region of interest drawn to compute accurately the vertical displacement of the indenter. The indenter's displacement was supposed to be equal to the maximum value of vertical displacement present among all the active subsets of this ROI.

```
for s=1:1:200 % all the DIC images taken during the test
    disp_y=handles_ncorr.data_dic.displacements(s).plot_v_ref_formatted;
    [m,n]=size(disp_y);
    k=1;

    for i=1:1:m
        for j=1:1:n
            % displacement is 0 if the subset is not active (outside the ROI)
            if(disp_y(i,j)~=0)
                % vector containing the vertical displacement of all the subsets of the s-th image
                v(k)=disp_y(i,j);
                k=k+1;
            end
        end
    end

    % vector containing the maximum displacement value of each vector v (i.e. each DIC image)
    V(s,1)=max(v(s));
end
```

Figure 42: Matlab code used to compute the indenter's displacement as the maximum vertical displacement of the ROI in fig.41.

Third Approach: Fitting of the Williams-Westergaard's Model

The current method was undertaken with the aim of avoiding the measurement of the lenght of the propagated crack. In fact, this step that has negatively influenced and compromised the success of the first two attempted computational strategies, was not required in this case.
The SIFs and the T-stress can be obtained by fitting the analytical equations of the Williams' expansion type with the experimentally-determined displacement fields. The results in terms of fracture mechanics parameters strictly depend on the dimension of the area considered around the crack tip in conjunction with the crack length, the maximum SIF (and thus the plastic tip radius), and the number of terms to be considered in the Williams-type expansion [34]. Special attention is required to properly select the DIC measurements. For example, the choice of the area of interest in front the crack tip (field-of-view) strictly depends on to the type of the analytical model selected for the fitting of the displacement field. In fact, real crack tip displacement fields are affected by several factors that cannot be easily controlled during DIC displacement measurements. Crack tip plasticity, crack closure, correlation parameters (field of view, subset size) have shown to profoundly influence the SIF calculation.
The authors of [34] focused on the analysis of the field-of-view influence in the SIF calculation from displacement fields measured using the DIC technique. This study provides a guideline to properly select the field-of-view dimension and the number of terms in the Williams expansion to obtain accurate SIF evaluation from DIC measurements. The regressions based on the Williams expansion of the displacement fields in front of the crack tip made adopting only the first term yield to precise SIF estimations only for very restricted field-of-view dimension d (less than $0.01mm$). However, the real material behavior shows local plasticity in front of the crack tip which includes the small area where the K regression provides accurate results. In addition, performing DIC measurements with such small field-of-view is a challenging task and it would involve other problems with out-of-plane displacements that affect the DIC quality. It turns out that the regression based only on the first term of the Williams expansion is not feasable, and the additional terms are required to be fitted. The SIF measurement based on the 2-terms regression was also observed to provide generally inaccurate SIF values. In particular, only for field-of-view dimensions lower than $d < 0.2mm$. The 3-terms regression resulted in the most stable and accurate SIF estimations giving an accuracy of less than 5% on the SIF estimation. The adoption of larger number of terms to fit the Williams expansion do not improve further the SIF accuracy.
A possible approach to tackle a linear elasticity problem using experimental data is to guess an analytical stress function, satisfying the boundary conditions, and determining the displacement and stress field analytically. These analytical fields can then be fitted

to the experimental data and the required parameters, for example, T-stress and stress intensity factor, can be determined [27]. In this case the experimental data are those related to the opening displacement field yielded by the DIC analysis carried out during the bending test. For this purpose the following setting parameters were adopted:

- ROI shape = Disc
- subset size = 17 pixels
- subsets spacing = 2 pixels

Coherently the analytical expression of the same opening displacement field has been formulated. For this purpose the Williams-Westergaard (WW)'s analytical solution has been exploited in order to extract K_{Ic} from the fitting with the experimental displacement data provided by DIC analysis. Some simplifications have been adopted in the mathematical model because they do not influence the validity of the proposed method and don't exert much influence on the outcomes of the computation. The focus was set mainly on the general process as computational tool, and not on the numerical results. In fact in this stage it was more important to the autors to show an indicative entity of the mechanical improvement rather then obtain very accurate final values for the two kind of specimens. It's easily predictable that it can be profitably applied in a more complete elastic model that would remove the following simplificative assumptions.
Though the presence of mode mixity in the fracture behavior, due not to the loading, which is purely tensile, but to the anisotropy of the material (in greater degree for the optimized configuration), only mode I has been taken into account in the calculation because the displacement field is strongly dominated by the tensile manner and very little influence is exerted by shear mode. Mixed mode displacement fields could anyway be derived by simply superimposing the mode I and II displacement fields, whose formulas are both considered in the WW model. Furthermore, the term related to the T-stress in the WW equations has been neglected because in a mode I loading case and for the given geometry its contribution is not of much relevance. Moreover the agreement between the numerical and experimental results obtained for the T-stress was not as good as for the stress intensity factor results. Compared to the stress intensity factor, the T-stress is the coefficient of higher order terms of the displacement field expansions, this makes the T-stress relatively a more difficult parameter to measure experimentally [27]. Lastly, only the opening displacement field, v, has been contemplated and used for the fitting procedure, because only for this one it was possible to easily remove the rigid body motion component from the DIC measured data. In fact, due to the antisymmetry of the v field within the Region of Interest (ROI) adopted in the DIC analysis (which instead is symmetrical with respect to the vertical load line as it possible to see in Fig. 43) it is possible to identify the rigid body motion with the average value of the field itself: the theoretical average v displacement of an area symmetrical with respect to the vertical load line should be null by definition during the three point bending test. So it has been sufficient to measure the average v displacement in the entire ROI, provocated by an horizontal slip of the specimen during the test, and subtract it from the displacement value of each subset of the ROI. Instead, for the vertical displacement component u, a robust method to calculate the rigid body motion is more complicated to find because the symmetry that characterizes it within the ROI doesn't allow to apply the same method (the average displacement in this case should not be equal to zero). The rigid body rotation is neglected because of the mode I case.

Following the WW model the displacement field ahead of a crack tip can be expressed as an infinite series. In a plane mode I condition this displacement field is expressed as

$$v_I = \sum_{n=1}^{\infty} \frac{r^{n/2}}{2\mu} a_n \left\{ \left[k - \frac{n}{2} - (-1)^n \right] \sin \frac{n\theta}{2} + \frac{n}{2} \sin \frac{(n-4)\theta}{2} \right\} \tag{24}$$

where v is opening (y direction) displacement in mode I, μ is the shear modulus and $k = (3-\nu)/(1+\nu)$, because of the plane stress conditions, where ν is the Poisson ratio, a is a constant and r and θ are radial and angular coordinates from crack tip.

By defining $f_{n,m}(r,\theta)$ and $g_{n,m}(r,\theta)$ as follows (Eqs.25,26), the displacement field (Eq.24) can be written in a matrix form (Eq.27)

$$f_{n,m} = \frac{r_m^{n/2}}{2\mu} \left\{ \left[k - \frac{n}{2} - (-1)^n \right] \sin \frac{n\theta_m}{2} + \frac{n}{2} \sin \frac{(n-4)\theta_m}{2} \right\} \tag{25}$$

$$g_{n,m} = \frac{r_m^{n/2}}{2\mu} \left\{ \left[k - \frac{n}{2} + (-1)^n \right] \cos \frac{n\theta_m}{2} + \frac{n}{2} \cos \frac{(n-4)\theta_m}{2} \right\} \tag{26}$$

$$\begin{pmatrix} v_1 \\ v_2 \\ \vdots \\ v_m \end{pmatrix} = \begin{pmatrix} f_{1,1} & f_{2,1} & \cdots & f_{n,1} & g_{1,1} & g_{2,1} & \cdots & g_{n,1} \\ f_{1,2} & f_{2,2} & \cdots & f_{n,2} & g_{1,2} & g_{2,2} & \cdots & g_{n,2} \\ \vdots & \vdots & \ddots & \vdots & \vdots & \vdots & \ddots & \vdots \\ f_{1,m} & f_{2,m} & \cdots & f_{n,m} & g_{1,m} & g_{2,m} & \cdots & g_{n,m} \end{pmatrix} \begin{pmatrix} a_1 \\ a_2 \\ \vdots \\ a_n \\ b_1 \\ b_2 \\ \vdots \\ b_n \end{pmatrix} \tag{27}$$

where m is the data point index.

By expanding Eq.24, omitting the terms of order $r^{3/2}$ and above and comparing with the more common notation, using the stress intensity factor as shown in the following equation,

$$v = \frac{K_I}{2\mu} \sqrt{\frac{r}{2\pi}} \cos \frac{\theta}{2} \left(k - 1 + 2 \sin^2 \frac{\theta}{2} \right) \tag{28}$$

it can be shown that:

$$K_I = a_1 \sqrt{2\pi} \tag{29}$$

in which K_I is the mode I stress intensity factor. Following this approach the SIF is simply function of a constant that can be easily calculated. There is no definite and univocal answer to the required number of terms of the equation to obtain the best fit for the experimental data, though an increasing precision can be expected with the addition of more terms. Hence, the number of terms should be increased until no substantial changes in the determined parameters are observed. In this case the first five terms were considered although already after two terms the results were fairly stable (more terms were needed instead to obtain stable values for the T-stress). Hence the Eq. 24 was expanded up to $n = 5$ and K_I, differently from Eq. 29, resulted to be function of constants a_1 to a_5 of Eq. 27. At this point the SIF value could theoretically be extrapolated from Eq.27: the matrix elements are known because they derive from the analytical model, the elements of the displacement vector are the experimental opening displacement components of each subset of the ROI and are provided by the DIC analysis. However, the matrix is not square and then the vector of the constants is not computable through a matrix inversion. To overcome this obstacle a reverse algorithm was adopted and it was applied a Monte Carlo method, a computational technique that with the proper calibration allows to estimate very precisely the SIF value.

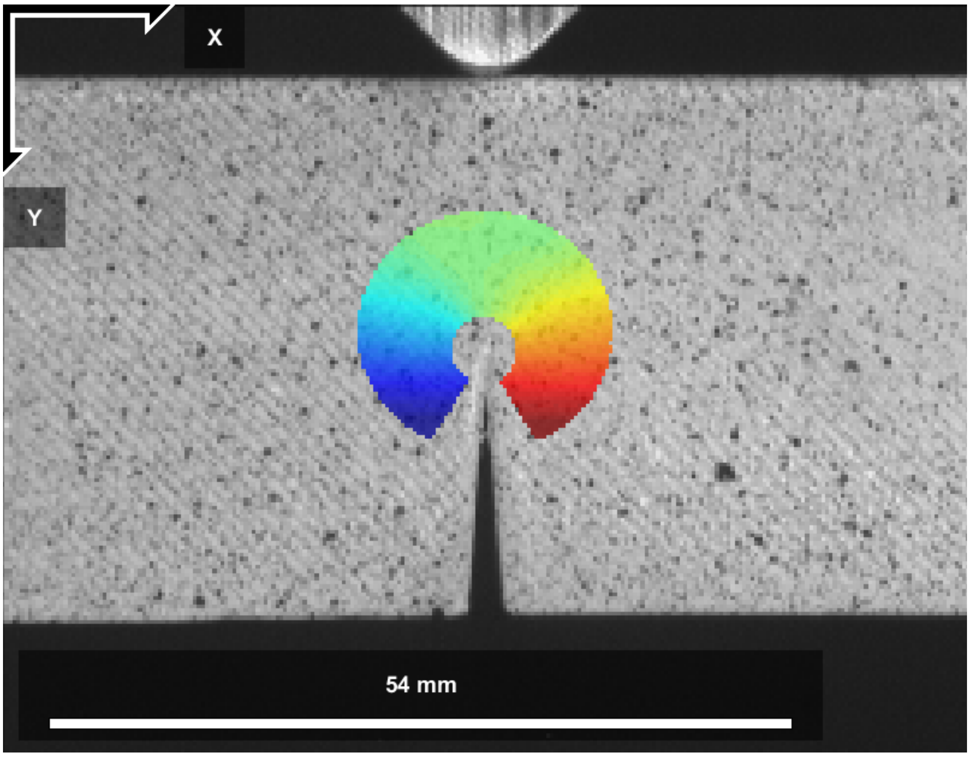

Figure 43: **Region of Interest for the SIF computation.** The symmetry of the ROI permitted to easily remove the horizontal rigid body displacement.

Monte Carlo Method

Monte Carlo methods are a broad class of computational algorithms that rely on repeated random sampling to obtain numerical results. The main idea is using randomness to solve problems that might be deterministic in principle and their implementation is most useful when it is difficult or impossible to use other approaches. In this case it was applied to the measurement of K_{Ic} to minimize the residue between the theoretical and the measured displacement field. Instead of calculating the constants' vector starting from the experimental displacement field and the anlytical model, the whole process was inverted. As it is possible to observe in Eq. 29, once the constant a is known, K_I is known too. With the Monte Carlo algorithm a random sampling of an interval of constants a_i was carried out. The aim is to find the solution that reduces as much as possible the residue (the difference between the measured and the guessed value). However, there is no guarantee that this method converges to the unique solution of the problem. For this reason, it is necessary to "help" the algorithm by choosing adequately and judiciously the initial guess and the interval of search. Thus, two methods can be used:

- The solution can be predicted using FEM simulation (K_I, K_{II} and T stress can be computed using J integral) and then be corrected by the MC algorithm.
- Prediction of the solution using non linear (NL) least square and, as before, correct the solution using MC algorithm.

Both methods are "prediction-correction" methods. The second was adopted in this case. About the interval of search there are no constraints: $+-50\%$ of the value predicted by NL least square was chosen to cover the solution fluctuation.

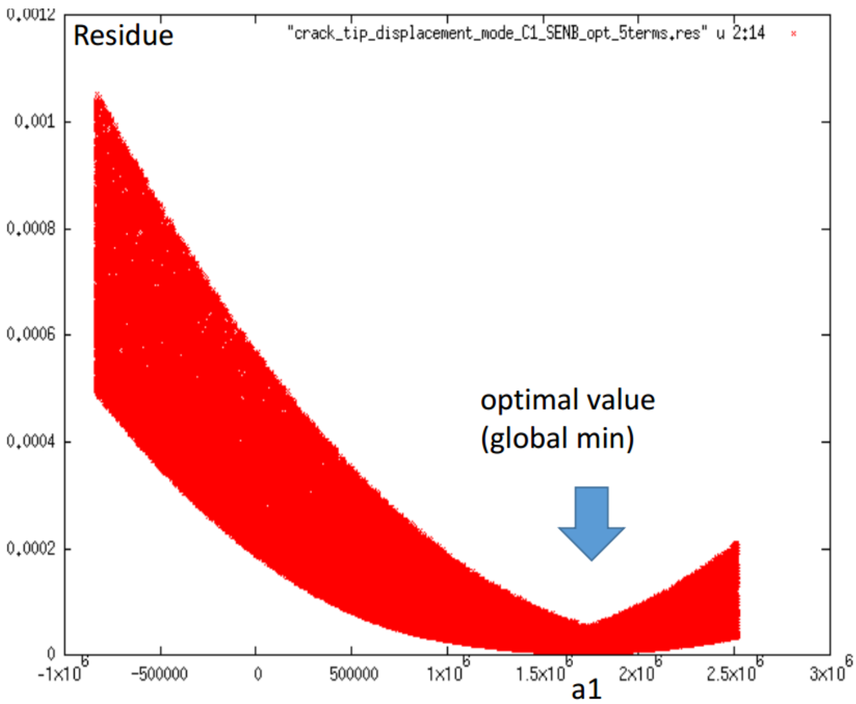

Figure 44: **Plot of residue versus constant a_1:** each marker corresponds to a random a_1 value selected within the scanning interval of the Monte Carlo method.

A $C{+}{+}$ code was used to implement this computation and thanks to its high computing performances the number of iterations of the sampling could be pushed up to $1e5$ attempts in order to obtain a very accurate estimation and an extremely little residual error.

In Fig. 44 are shown all the attempted values for constant a_1. For each of those the code computed the entire analytical displacement field and then the residual values were calculated as follows:

$$residue = \sum_{i=1}^{N} (v_{DIC} - v_{MC})^2 \tag{30}$$

with N being the number of subsets included in the ROI and v_{DIC} and v_{MC} being, respectively, the subset's displacement measured by DIC and the subset's displacement calculated with the attempted a_i values.

The next step is to use the attempted a_i values that produce the minimum residue (Fig. 44) to calculate the best approximation of K_{Ic}, the optimal K_{Ic}. Furthermore, now the matrix operation (Eq. 27) can be completed and a numerical v displacement field is gathered. Being computed starting from the optimal value of K_{Ic}, it is referred to as optimal displacement field and is the numerical field that best approximates the experimental DIC field (Fig. 45).

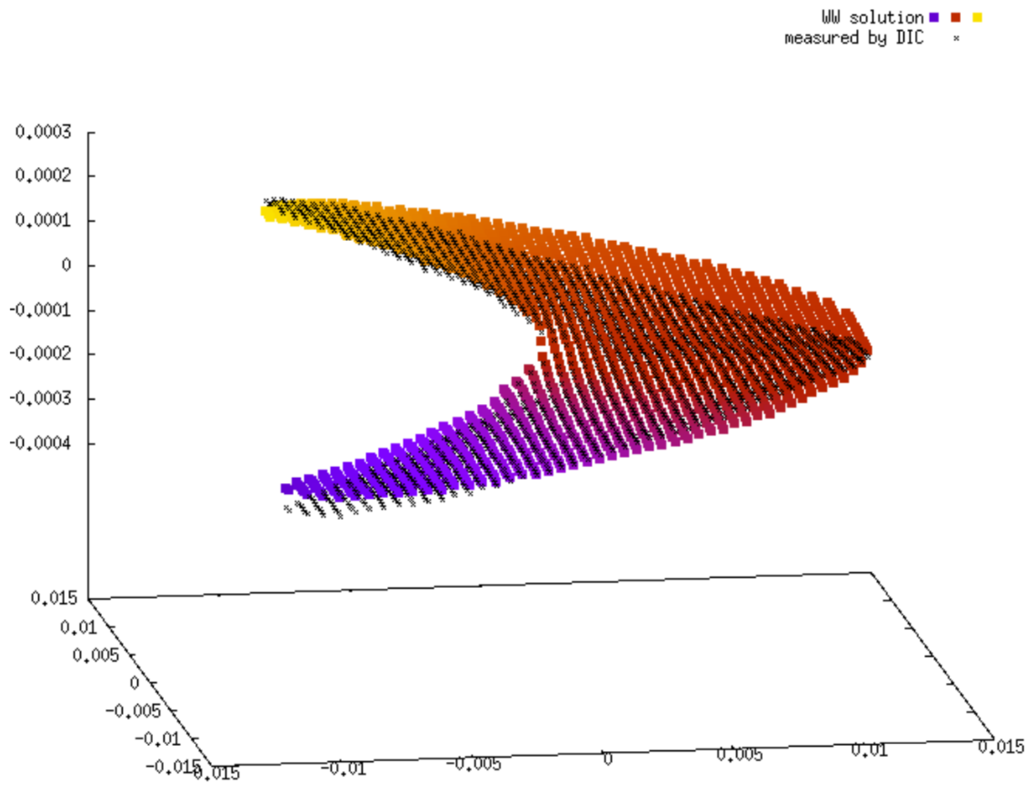

Figure 45: **Numerical and measured displacement fields.** The numerical displacement is provided by the implementation of the Williams-Westergaard model with the optimal K_{Ic} yielded by the Monte Carlo method. The other field, represented by black markers, is the opening displacement measured by DIC analysis.

To employ this method to calculate of the critical stress intensity factor K_{Ic}, in order to measure the fracture toughness of the specimens, it was necessary to apply it to the displacement field measured in correspondance of the crack onset. Hence, the preliminar information that was required was which DIC image was the one that captured the very first crack opening around the notch tip. In fact the fracture toughness of an elastic material in a mode I loading case is identified as the value of K_I at the moment in which the crack starts to propagate, which is K_{Ic}. To detect as accurately as possible this crucial event, a DIC-based method was exploited and a specific matlab script has been written with the aim of investigating the opening displacement field characterizing a new small ROI set in the vicinity of the notch tip.

Crack Onset Detection

DIC based method

In this section the method used to identify the moment of the crack onset through a new specific DIC analysis will be shown. The technique consists in extracting from the ROI and processing only a few small groups of subsets and plot the related variables, yielded from the DIC analysis, versus the snapshot number. These variables are horizontal (opening) displacement, v, horizontal strain, ε_{yy}, and correlation coefficient (CC). The purpose is to detect, through the observation of the variables' trend, the crack onset and therefore the material opening, with the associated CC increase. In fact the CC value is directly proportional to the difficulty that the DIC software, Ncorr in this case, encounters when it must correlate the same subsets between two successive images. This implies that the CC value increases in case of high deformation of the subsets, a condition that is logically expected to happen before the crack propagation onset.

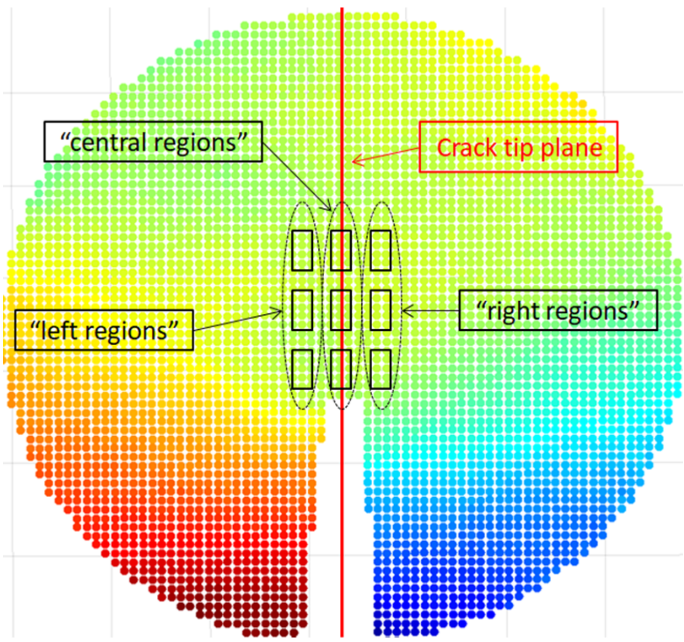

Figure 46: **ROI and the groups of subsets processed with matlab to detect the crack onset.** Disposition of the regions analyzed in the final method adopted to detect the crack's onset.

The groups of subsets must be selected usefully and in a reasoned manner in order to extract from them informations as clear as possible. The crack path has been visually predetermined from the DIC images and the position of the inestigated subsets is optimized in function of that in order to get more easily interpretable results. Moreover, the areas of the ROI to analyze were selected differently dependently by the particular specimen under exam and the specific variable of interest. When the focus was set on the examination of the horizontal displacement and horizontal strain they were positioned on the sides of the expected crack path (Fig. 49) to use the divergence of behavior after the material opening as a detecting tool (the region on the left of the crack is expected to increase the displacement value, the opposite for the region on the right side). To study the trend of the CC in a useful manner the regions were located along the exected crack path (Fig. 48) in order to analyze the slopes' increase in the plots, which can be interpreted as a sign of high deformation happening. On average this small regions were constituted by 6 to 9 subsets each and the mean value of the variable under exam was computed before plotting it versus the snapshot number.

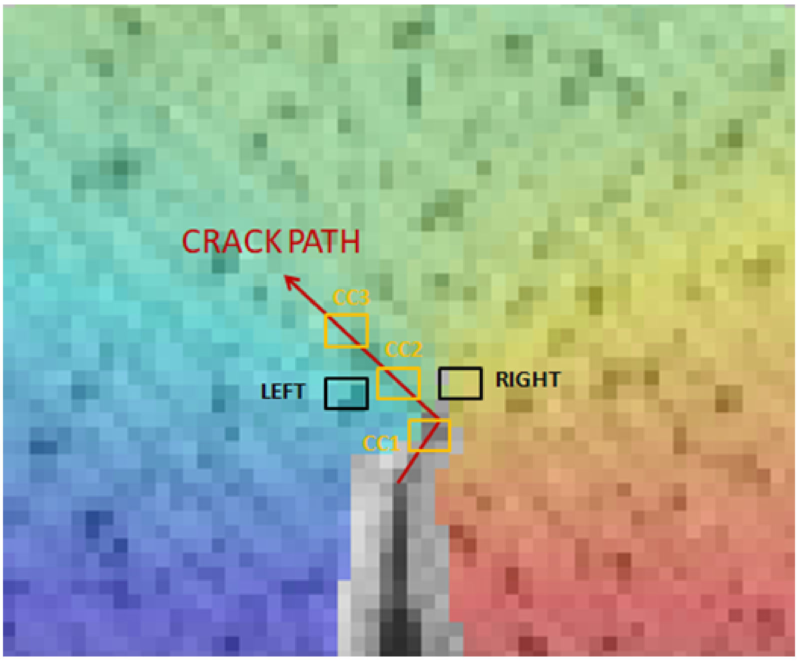

Figure 47: The aim is to determine the moment in which data belonging to different subsets start to show a divergent behavior. Tracking the data evolution of strategically positioned areas allows to detect the onset of the crack in the notch tip proximity.

```
clearvars -except handles_ncorr

x_tip = 120; % specimen's tip coordinates [subset]
y_tip = 89;

for s=1:1:200 % snapshots computed

    % extract DIC data
    scale = handles_ncorr.data_dic.dispinfo.pixtounits; % [mm]
    spacing = handles_ncorr.data_dic.dispinfo.spacing; % 2
    corel_coef = handles_ncorr.data_dic.displacements(s).plot_corrcoef_dic;
    disp_x = handles_ncorr.data_dic.displacements(s).plot_u_ref_formatted*0.001; % [m]
    exx = handles_ncorr.data_dic.strains(s).plot_exx_ref_formatted;

    % CC notch tip area and residual ROI
    corel_coef_tip = corel_coef(92:95,124:125); % (y,x)
    cc_tip(s) = mean(nonzeros(corel_coef_tip));
    corel_coef_roi = corel_coef;
    corel_coef_roi(92:95,124:125) = 0;
    cc_roi(s) = mean(nonzeros(corel_coef_roi));

    % Opening displacement and exx strain
    u_left(s) = mean(nonzeros(disp_x(92:95,121:123)));
    u_right(s) = mean(nonzeros(disp_x(92:95,126:128)));
    RB_disp(s) = mean(nonzeros(disp_x)); % rigid body displacement
    u_left_wrb(s) = u_left(s) - RB_disp(s);
    u_right_wrb(s) = u_right(s) - RB_disp(s);
    exx_left(s) = mean(nonzeros(exx(90:92,122:123)));
    exx_right(s) = mean(nonzeros(exx(90:92,127:128)));

    % CC in sequential crack stages
    cc1(s) = mean(nonzeros(corel_coef(92:94,123:124)));
    cc2(s) = mean(nonzeros(corel_coef(87:89,123:124)));
    cc3(s) = mean(nonzeros(corel_coef(80:83,113:115)));

    % Displacement of peak CC subset
    [m,n] = size(corel_coef); % matrix representing the entire DIC image
    k = 1;
    for i=1:1:m
```

```
        for j=1:1:n
            if(corel_coef(i,j)~=0) % it's equal to zero if it's outside the ROI

                Y(k) = (i-1)*spacing*scale; % from matrix indices to mm
                X(k) = (j-1)*spacing*scale;
                Co(k) = corel_coef(i,j);
                k = k+1;

            end
        end
    end

    % notch tip taken as the new origin
    ori_x = (x_tip-1)*spacing*scale;
    ori_y = (y_tip-1)*spacing*scale;

    % new coordinates
    Yc = Y - ori_y;
    Xc = X - ori_x;

    % axes inversion
    x = -Yc;
    y = -Xc;

    % polar coordinates
    R = sqrt((x.*x)+(y.*y));
    theta = atan2(y,x);

    [Co_max, iCo] = max(Co);
    CC(s) = Co_max; % peak CC value
    R_CC(s) = R(iCo); % peak CC radius
    theta_CC(s) = theta(iCo); % peak CC angle
end
```

Outcomes' Analysis

In all the tests that were carried out in this study three different matlab scripts were employed to detect the crack onset. In all cases they resulted to be in pretty good agreement with each other and yielded a stable and apparently reliable snapshot range for the crack onset. The first script, and the related plot (Fig. 48), is meant to analyze the trend of the mean CC of three groups of subsets placed sequentially along the expected crack path. It could also be updated and calibrated in order to measure the crack growth rate and the crack lenght by mean of the investigation of the rearing's lag between the curves. In this case, where the interest is on the crack onset, only the curve referred to "area 1" was relevant: the complete plot was carried out only to have a visual confirm of the reliability of the assumption made and the right functioning of the matlab script adopted. The CC value that seems to correspond to a material separation it has been in all cases about 0.5.

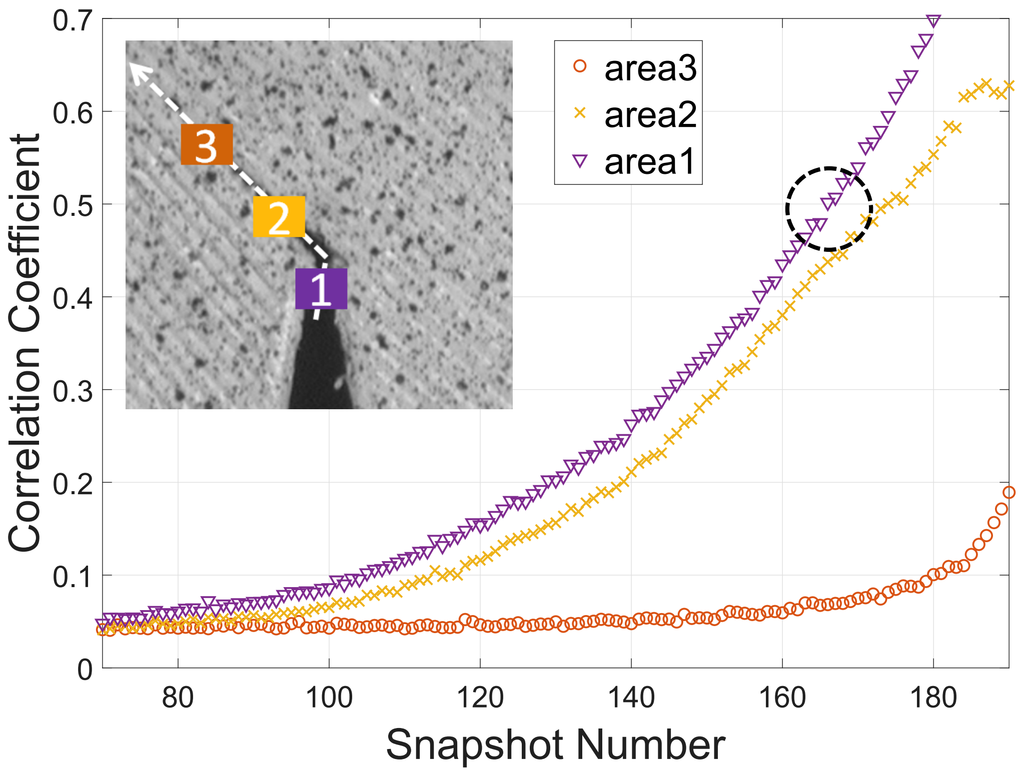

Figure 48: **Correlation coefficient along the crack path.** The curves represent the trend of the average correlation coefficient value of three areas located along the crack path and are indicative of the progress of the crack. The value that resulted to be symptomatic of the crack opening is about 0.5 (black dashed circle).

With the second script, and the related plot (Fig. 49), the trend of both horizontal displacement and horizontal strain was studied. The snapshot range that pointed to the crack propagation's start was identified in a sudden slope change in the displacement curve and with the reaching of the maximum in the strain curve. Both resulted in a very good agreement. The rapid strain decrease means that the force applied by the opposite face of the crack is decreased because of material separation and therefore a partial elastic recover is expected in this area. In addition to this, there is a loss of data due to pixels deactivation in presence of a marked discontinuity: with the crack onset the CC value of some subsets reach saturation and as a consequence the subset switches off and yields zero as a value for every analyzed variable and get excluded by the mean value computation. This means that the mean value, prived of the highest CC values, decreases. A displacement increase confirm what was expected for the left side, which after the crack opening, starts to slide towards greater y values. The opposite behavior was expected for the right side.

In the third script, and related plot (Fig. 50), the focus of the investigation was set on the displacement of the subset presenting the maximum CC value within the entire ROI. The localization of its position was expressed in terms of polar coordinates with a reference frame set in the notch tip. Hence, the radial and angle coordinates with resect to the notch tip and the notch front's plane were measured. Mean CC value of the ROI and peak CC value were plotted too, in order to verify the expected divergence between these two curves.

The goal is to track the crack front displacement following the displacement of the peak CC value. In fact, the assumption is that the area which is immediately forward to the crack front should be the one characterized by the highest CC value. For every test the first 50 to 80 snapshots are characterized by very unstable data for what concerns radius and angle plots: this can be interpreted as an indicator of the fact that noisy data around the whole ROI are still responsible for CC values higher than the CC value yielded from the notch tip area. This means that close to the notch tip there is not a prominent increase of CC yet, and therefore the deformation is not evident. The position of the peak CC continuosly changes in this part of the graph, popping out in random spots that are usually close to the ROI border. This assumption seems to be confirmed by the almost unperceptible difference between the peak CC and mean CC curves in this initial part of the plot. After instead, it is possible to notice a net divergence between the two of them. When the radius and angle curves stabilize and drastically decrease their absolute value it means that the highest CC, and consequently the highest deformation, is in the notch tip area. From now on the curves represent the CC trend of the notch tip area. In the optimized specimens the plots remain partially unstable also after the central part of the graph because the material deforms and separates not properly in proximity of the notch tip but, also simultaneously, in multiple spots along the weaker welding lines. The snapshot range was selected where CC reaches 0.5 and the radius presents a very tiny value.

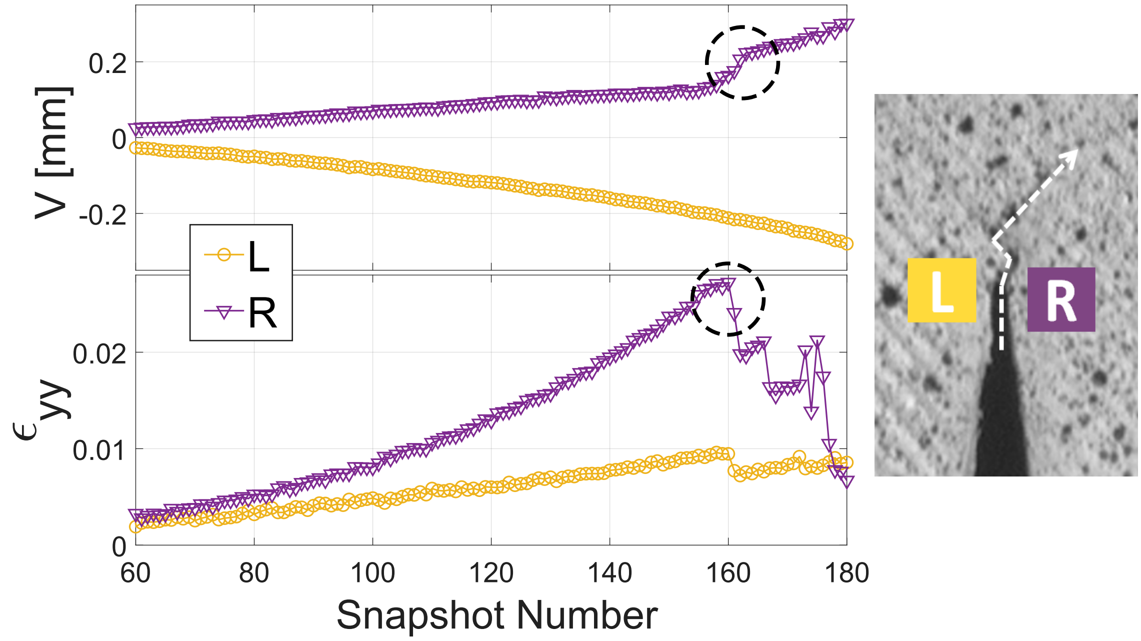

Figure 49: **Top**: opening displacement beside the crack. The fracture provokes a sudden slope change. **Bottom**: horizontal strain beside the crack. The fracture has been identified in correspondance of the peak.

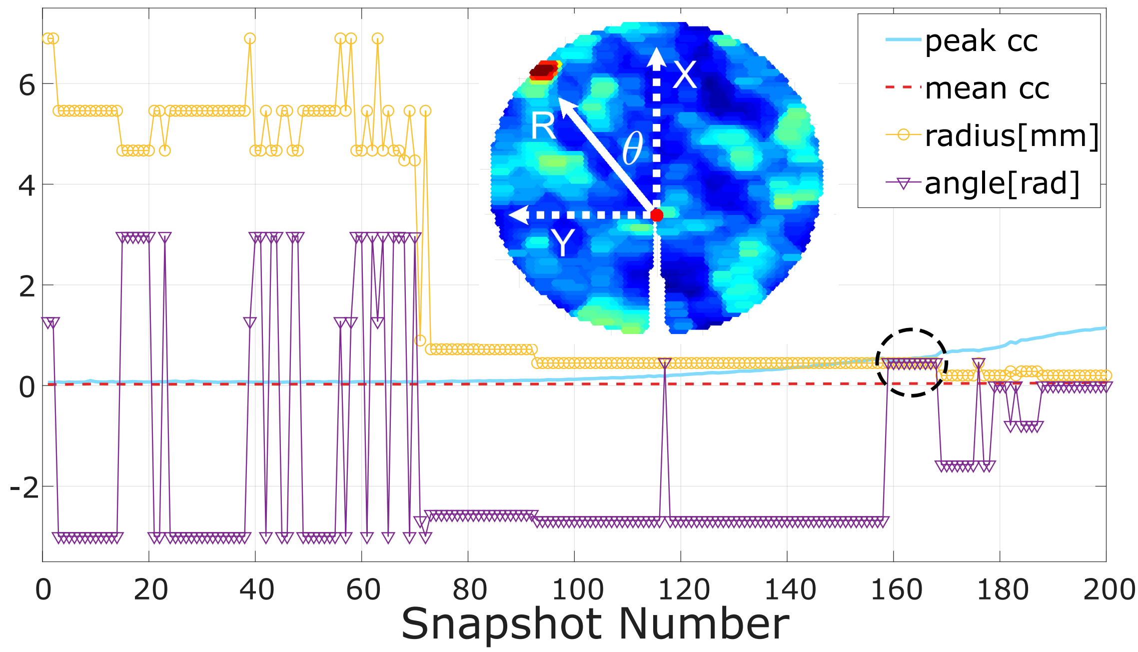

Figure 50: **Displacement of the peak correlation coefficient value.** The aim is to track the crack front displacement following the displacement of the peak value of the correlation coefficient. The assumption is that the area immediately ahead of the crack front presents the highest value.

Results

Crack Onset

The three crack onset detecting methods always resulted to be in good agreement and pointed out to the same snapshot range. Anyway it doesn't seem to the autors that this method could guarantee enough precision to identify the exact moment of the crack start in a particular snapshot. Hence, in this work a range of 10 snapshots in which it is possible to say with a very high degree of confidence that the crack onset surely happens has been identified for every tested specimen. Therefore, an average SIF of the range has been computed in order to get a statistical comparison between the specimens instead that a precise value for each sample.

The following snapshot ranges were extrapolated for the six samples tested:

	Snapshot Range
C1	170-179
C2	155-164
C3	165-174
Opt1	140-149
Opt2	165-174
Opt3	140-149

Table 7: Crack onset's detection data for the tested specimens: 3 classical (C) and 3 optimized (Opt). For each sample a 10 images range was selected.

These ranges were converted in a value of the indenter's displacement through the time law of the deformation imposed during the test and the frequency of image acquisition of the camera. Afterward the obtained values were reported in the force-displacement curve of the bending test to see how the detected crack onset was located with respect to the maximum force value. As it is possible to observe in Fig. 51, the snapshot ranges were found always in the close proximity of the maximum of the curves, with the exception of one case. This is a further confirm that the detecting method can be considered fairly reliable. The specimen which presented the odd result is one of the optimized beams. This makes sense because those were the specimens more likely to present an hardly predictable behavior, due to the not homogeneus and gradual opening of the material which characterises them. In fact, it is possible that the rectangular regions (Fig. 47) , used to analyze the trends of the variables observed to detect the crack onset, were not adequately positioned in this case and could not predict the actual behaviour of the specimen, missing the spot where the first crack appears.

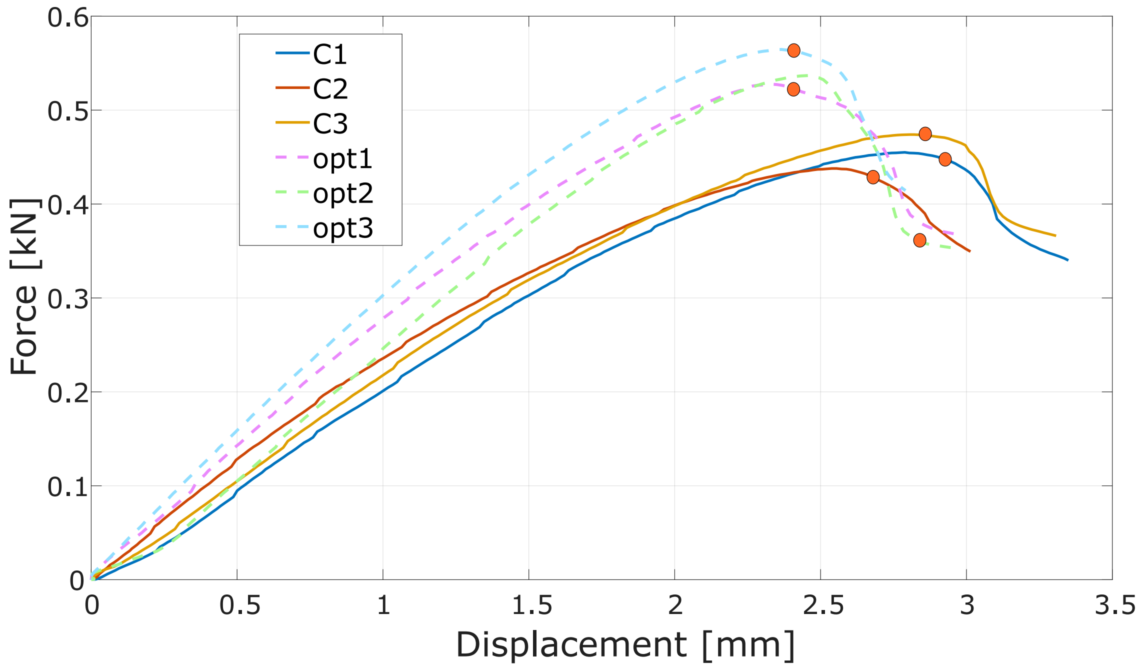

Figure 51: **Mechanical test.** The crack onset was detected almost precisely in correspondance of the peak force value. The only exception is specimen opt2 (the onset is detected when the applied force is already drastically decreased and the specimen should be already broken).

SIF comparison

The Poisson ratio and Young modulus considered in this last calculation are those of homogenous ABS ($E = 1.2MPa$, $\nu = 0.35$) for both classical and optimized specimens, hence a little overestimation of all the final numeric values is expected because a stronger material structure is supposed. The results referred to only one snapshot (the central one) belonging to the chosen range for every specimens are reported in this section. The other snapshots, being close to each other and belonging to the very same phase of the bending test, yield very similar results. The lowest value of K_{Ic} of the optimized specimens is always higher of the highest value of the classical specimens. The average improvement obtained with this optimization in term of stress intensity factor for a mode I loading case is about almost 15%.

Critical SIF MC simulation	
Classical Samples	$MPa \cdot \sqrt{m}$
C1	4.34
C2	4.75
C3	5.05
C average	4.71
Optimized Samples	
Opt1	5.28
Opt2	5.57
Opt3	5.30
Opt average	5.38
% improvement	14.2

Table 8: Stress intensity factor yielded from the Monte Carlo method for the 6 bending specimens: 3 classical (C) and 3 optimized (Opt).

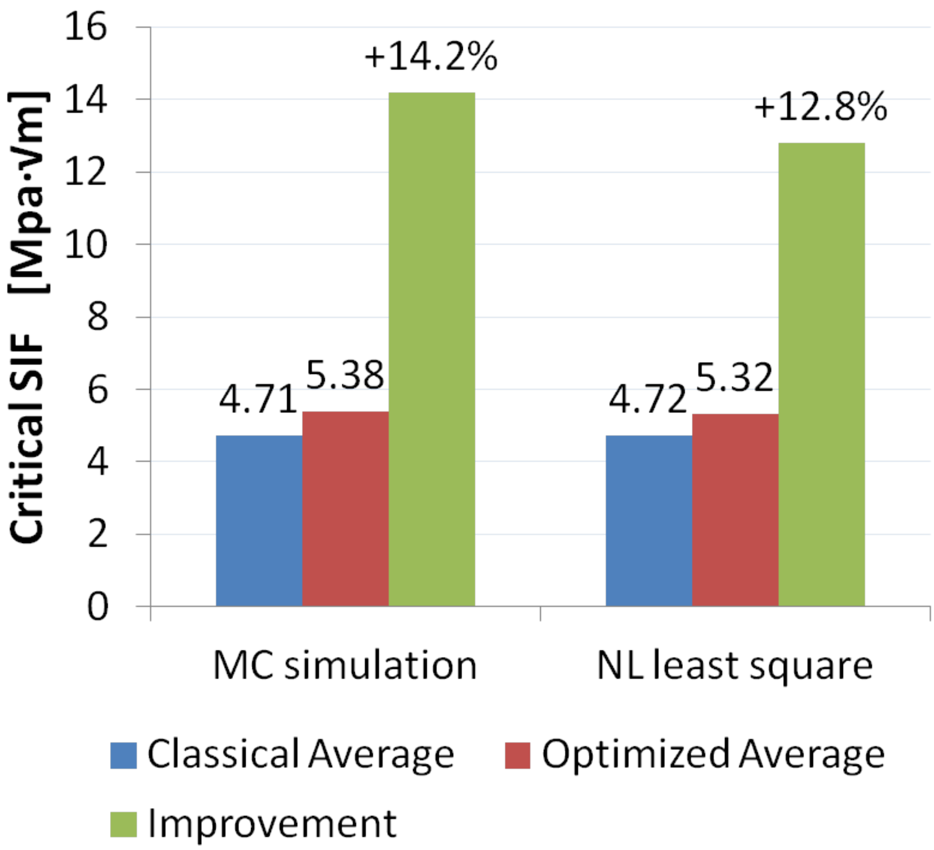

Figure 52: Stress intensity factor yielded from the Monte Carlo method for the 6 bending specimens: 3 classical (C) and 3 optimized (Opt). On the right also the values obtained with the non linear least square analysis is reported.

Conclusion

The mechanical test shows that an actual improvement of the mechanical resistance can be observed in the first part of the force-displacement curves. The slope is in fact steeper, which is a sign of increased resistance and stiffness. Also the maximum force is higher, which means that in order to break the optimized specimens the bending machines had to apply an higher load (in fact the crack onset has been detected very close to the peak force value). The optimized specimens crack, on average, at a smaller snapshot number, which means at shorter time and then in correspondance of a smaller indenter's displacement. While the maximum force during the test is higher for the optimized ones, the maximum displacement is higher for the classical ones, probably due to the fact that the optimized specimens present a collapse in presence of welding defects.
Although the comparison between the classical and the optimized specimens could seem improper because they don't break in the same fashion (optimized never brake in the notch tip) this doesn't affect the validity of the study. On the contrary, it testifies that the potential enhancement due to the optimization of the filament deposition could also be stronger in absence of the welding flaws. In fact the failure far from the notch tip doesn't allow to reach the load that would be able to break the optimized specimens in the notch tip as the classical ones. It's reasonable to expect that, using a stronger kind of extrusion material (like metal) or a more precise printing machine able to avoid these printing defects and air gaps, the effects of this innovative optimization could result in even better improvements.

Bibliography

[1] J. Gardan, A. Makke, N. Recho, A Method to Improve the Fracture Toughness Using 3D Printing by Extrusion Deposition, 21st European Conference on Fracture, ECF21, 20-24 June 2016, Catania, Italy

[2] P.Lanzillotti, J.Gardan, A.Makke, N.Recho,"*Strengthening in fracture toughness of a smart material manufactured by 3D printing*", IFAC PapersOnLine 51-11 (2018) 1353–1358.

[3] K. Tohgo, H. Ishii, "*Elastic-plastic fracture toughness test under mixed mode I-II loading*", Engineering Fracture Mechanics (1992), vol. 41, No. 4, pp.529-540.

[4] J. Gardan, International Journal of Production Research **54**(10), 3118 (2016)

[5] Avaible at: *https://wohlersassociates.com/press63.html*, visited: 09/05/2017

[6] J.Gardan,"*Additive manufacturing technologies: state of the art and trends*", International Journal of Production Research 54 (2015) 3118–3132.

[7] B.N.Turner, R.Strong, S.A.Gold,"*A review of melt extrusion additive manufacturing processes: I. Process design and modelling*", Rapid Prototyping Journal (2014), Vol. 20 Issue: 3, pp.192-204,

[8] H. Bikas, P. Stavropoulos, G. Chryssolouris, "*Additive manufacturing methods and modelling approaches: a critical review*", Int J Adv Manuf Technol (2016) 83:389–405.

[9] A. Nycz, A. I Adediran, M. W. Noakes, L. J. Love, "*Large Scale Metal Additive Techniques Review*", Solid Freeform Fabrication 2016: Proceedings of the 27th Annual International Solid Freeform Fabrication Symposium – An Additive Manufacturing Conference.

[10] Bellini, Anna and Güçeri, Selçuk,"*Mechanical characterization of parts fabricated using fused deposition modeling*", Rapid Prototyping Journal (2003), vol. 9, No. 4, pp.252-264.

[11] G. S. Bual, P. Kumar, "*Methods to Improve Surface Finish of Parts Produced by Fused Deposition Modeling*", Manufacturing Science and Technology 2(3): 51-55, 2014.

[12] J. Martínez, J.L. Diéguez, A. Pereira, J.A.Pérez, "*Modelization of Surface Roughness in FDM Parts*", AIP Conf. Proc. 1431, 849 (2012).

[13] P. M. Pandey, N. V. Reddy, S.G. Dhande, "*Improvement of surface finish by staircase machining in fused deposition modeling*", Journal of Materials Processing Technology 132 (2003), 323-331.

[14] R. Anitha, S.Arunachalam, P. Radhakrishnan, "Critical parameters influencing the quality of prototypes in fused deposition modelling", Journal of Materials Processing Technology 118 (2001), 385-388.

[15] Lee, BH and Abdullah, J and Khan, ZA,"*Optimization of rapid prototyping parameters for production of flexible ABS object*", Journal of materials processing technology (2005) vol. 169, No. 1, pp.54-61.

[16] Montero, Michael and Roundy, Shad and Odell, Dan and Ahn, Sung-Hoon and Wright, Paul K,"*Material characterization of fused deposition modeling (FDM) ABS by designed experiments*", Society of Manufacturing Engineers (2001), vol. 10.

[17] J.F.Rodríguez, J.P.Thomas, J.E. Renaud,"*Mechanical behavior of acrylonitrile butadiene styrene (ABS) fused deposition materials. Experimental investigation*", Rapid Prototyping Journal, vol.7, no.3, pp.148–158, 2001.

[18] S.H.Ahn, M.Montero, D.Odell, S.Roundy, P.K.Wright,"*Anisotropic material properties of fused deposition modeling ABS*", Rapid Prototyping Journal, vol. 8, no. 4, pp. 248–257, 2002.

[19] G.C.Onwubolu,F.Rayegani,"*Characterization and Optimization of Mechanical Properties of ABS Parts Manufactured by the Fused Deposition Modelling Process*", International Journal of Manufacturing Engineering Volume 2014, Article ID 598531.

[20] J.Li, S.Yang, D.Li, V.Chalivendra,"*Numerical and experimental studies of additively manufactured polymers for enhanced fracture properties*", Engineering Fracture Mechanics (2018), doi: https://doi.org/10.1016/j.engfracmech.2018.11.001

[21] A. K. Sood, R.K. Ohdar, S.S. Mahapatra, "*Parametric appraisal of mechanical property of fused deposition modelling processed parts*", Materials and Design 31 (2010), 287–295.

[22] Ma F, Deng X, Sutton MC, Newman Jr JC., "*A CTOD based mixed mode fracture criterion. Mixed Mode Crack Behavior*", ASTMSTP 1999;1359:86–110.

[23] J. Li, X.B. Zhang, N. Recho, "*J-Mp Based Criteria for Bifurcation Assessement of a Crack in Elastic-Plastic Materials under Mixed Mode I-II Loading*", Engineering Fracture Mechanics, Vol. 71 (3), pp. 329-343, February 2004.

[24] R.Rezaie, M.Badrossamay, A.Ghaie, H.Moosavi,"*Topology Optimization for Fused Deposition Modeling Process*", Procedia CIRP (2013), vol. 6, No. Supplement C, pp.521-526.

[25] Prall, D and Lakes, RS,"*Properties of a chiral honeycomb with a Poisson's ratio of—1*", International Journal of Mechanical Sciences (1997), vol. 39, No. 3, pp.305-314.

[26] Galantucci, LM and Lavecchia, F and Percoco, G,"*Study of compression properties of topologically optimized FDM made structured parts*", CIRP Annals-Manufacturing Technology (2008), vol. 57, No. 1, pp.243-246.

[27] J.R. Yates, M. Zanganeh, Y.H. Tai,"*Quantifying crack tip displacement fields with DIC*", Engineering Fracture Mechanics 77 (2010) 2063–2076.

[28] M.Subramanyam Reddy, K.Ramesh, A.Thiyagarajan,"*Evaluation of mode-I SIF, T-stress and J-integral using displacement data from digital image correlation* ", Theoretical and Applied Fracture Mechanics 96 (2018) 146–159.

[29] Shun-Fa Hwang, Min-Chien Shen, Bin-Bin Hsu, "*Strain measurement of polymer materials by digital image correlation combined with finite-element analysis*", Journal of Mechanical Science and Technology 29 (10) (2015) 4189 4195.

[30] http://www.ncorr.com tabs crack-tip-experiments and dic-algorithms visited: 30/06/2017.

[31] N.McCormick, J. Lord, "*Digital Image Correlation*", Materials today, volume 13, number 12, December 2010.

[32] T.H.Becker, M.Mostafavi, R.B.Tait, T.J.Marrow,"*An approach to calculate the J-integral by digital image correlation displacement field measurement*", Fatigue & Fracture of Engineering Materials & Structures, October 2012.

[33] J.W.Hutchinson, Z.Suo,"*Mixed Mode Cracking in Layered Materials*", Advances in Applied Mechanics, Volume 29.

[34] S.Beretta,L.Patriarca,S.Rabbolini,"*Stress Intensity Factor calculation from displacement fields*", S.Beretta et alii, Frattura ed Integrità Strutturale, 41 (2017) 269-276.

[35] "*Standard Test Method for Measurement of Fracture Toughness*", ASTM International, Designation: E1820 – 11.

Acknowledgments

I would like to thank Prof. Brusa, Prof. Gardan, Prof. Makke and Prof. Recho who followed me during this work. They kindly passed to me their knowledge and, with their experience, they guided me through a process of learning. I feel grateful to them as well for passing down to me a great passion for scientific research and love for engineering.

A special thanks goes to my parents, who allowed me to always have the best academic education and provided me everything I needed in life. They have been giving me an excellent personal education and they have always supported me, no matter what. Thanks Mom and Dad for everything.

Finally, I would like to thank Flavia for the love and patience she has shown during these challenging years that have led us to be apart from each other longer than we wanted.